

July 25, 2024

Differential Effects of Sequence-Local versus Nonlocal Charge Patterns on Phase Separation and Conformational Dimensions of Polyampholytes as Model Intrinsically Disordered Proteins

Tanmoy PAL,^{1,†} Jonas WESSÉN,^{1,†} Suman DAS,^{1,2,†} and Hue Sun CHAN^{1,*}

¹Department of Biochemistry, University of Toronto, Toronto, Ontario M5S 1A8, Canada

²Department of Chemistry, Gandhi Institute of Technology and Management,
Visakhapatnam, Andhra Pradesh 530045, India

To appear in "J. Phys. Chem. Lett."

†Contributed equally.

*Correspondence information:

Hue Sun CHAN. E-mail: huesun.chan@utoronto.ca

Tel: (416)978-2697; Fax: (416)978-8548

Department of Biochemistry, University of Toronto, Medical Sciences Building – 5th Fl.,
1 King's College Circle, Toronto, Ontario M5S 1A8, Canada.

Abstract

Conformational properties of intrinsically disordered proteins (IDPs) are governed by a sequence-ensemble relationship. To differentiate the impact of sequence-local versus sequence-nonlocal features of an IDP's charge pattern on its conformational dimensions and its phase-separation propensity, the charge "blockiness" κ and the nonlocality-weighted sequence charge decoration (SCD) parameters are compared for their correlations with isolated-chain radii of gyration (R_g s) and upper critical solution temperatures (UCSTs) of polyampholytes modeled by random phase approximation, field-theoretic simulation, and coarse-grained molecular dynamics. SCD is superior to κ in predicting R_g because SCD accounts for effects of contact order, i.e., nonlocality, on dimensions of isolated chains. In contrast, κ and SCD are comparably good, though nonideal, predictors of UCST because frequencies of interchain contacts in the multiple-chain condensed phase are less sensitive to sequence positions than frequencies of intrachain contacts of an isolated chain, as reflected by κ correlating better with condensed-phase interaction energy than SCD.

Extensive recent research has elucidated myriad properties of biomolecular condensates and their essential roles in diverse biological functions (reviewed, e.g., in refs. 1, 2). These membraneless compartments are underpinned to a significant degree by liquid-liquid phase separation (LLPS) of intrinsically disordered proteins (IDPs), though more complex thermodynamic processes such as gelation/percolation and dynamic mechanisms— involving not only IDPs but folded protein domains as well as nucleic acids—also contribute prominently.^{3–5} The propensity for an IDP to undergo LLPS is dependent upon its sequence of amino acids.^{6–8} Many IDPs are enriched in charged and aromatic residues. Accordingly, beside π -related interactions,^{9–12} electrostatics is an important driving force for many aspects of IDP properties, as exemplified by its notable roles in IDP conformational dimensions,^{13,14} the stability of biomolecular condensates,^{6,15} and a condensate’s capability to selectively recruit IDPs with different sequence charge patterns.¹⁶

An IDP can exist and function as essentially isolated chain molecules and/or collectively in a multiple-chain condensate, or certain intermediate oligomeric configurations in between. With this in mind, analyzing the relationship between the behaviors of isolated and condensed IDPs is instrumental not only for inferring condensed-phase properties from those of computationally and experimentally simpler isolated-chain systems. More fundamentally, it offers insights into how sequence-encoded IDP properties are modulated by IDP concentration. For homopolymers with short-spatial-range interactions, it has been known since the 1950s via the Flory-Huggins (FH) theory that the radius of gyration R_g of an isolated polymer anticorrelates with the polymer’s LLPS propensity. This is because R_g decreases monotonically with the FH $\chi(T)$ interaction parameter¹⁷ at a given absolute temperature T and the LLPS critical temperature¹⁸ $T_{\text{cr}}^{\text{FH}}$ increases with $\chi(T)$ when the interactions are purely enthalpic, i.e., $\chi(T) \sim 1/T$ and thus $T_{\text{cr}}^{\text{FH}} = T\chi(T)/\chi_{\text{cr}}$ where $\chi_{\text{cr}} = (1 + 1/\sqrt{N_p})^2/2$ and N_p is polymer chain length,¹⁹ as is verified by recent simulations and more sophisticated polymer theories.^{20,21} Inspired by recent interest in sequence-specific IDP LLPS, similar relationships for heteropolymers are predicted between LLPS propensity and isolated-chain R_g (ref. 22), coil-globule transition,²³ and two-chain association in a dilute solution.²⁴ Likewise, dilute-phase R_g and demixing temperature was seen to correlate experimentally for variants of the P domain of core stress-granule marker polyA-binding protein undergoing heat-induced LLPS.²⁵

The predicted dilute/condensed-phase correlations for heteropolymers are significant but not perfect,^{22,23} as underscored by a recent extensive simulation study of the human proteome.²⁶ The imperfection is instructive about the physical chemistry of concentration-dependent IDP interactions. We focus here on electrostatics as a first step. Building on the substantial recent works on polyampholyte configurations and LLPS,^{13,14,22,27–30} we attend to a hitherto less explored consequence of sequence specificity, namely how the impact of sequence-local patterns involving charges proximate to one another differs from that of sequence-nonlocal patterns encompassing charges far apart along the chain. The differing effects of local versus nonlocal interactions has long been recognized in globular

proteins. These include folding stability³¹ and the effects of intrachain contact order³² on conformational ensembles as well as folding kinetics.^{33–36} But much about the corresponding effects for IDPs remains to be elucidated. To make progress, here we contrast the predictive powers of two common sequence charge parameters, namely the “blockiness” measure κ (ref. 13) and “sequence charge decoration” (SCD, ref. 14). For a N_p -bead polyampholyte with charge sequence σ_α ($\alpha = 1, 2, \dots, N_p$), κ captures primarily sequence-local aspects of the charge pattern as its terms account for charge asymmetry only in blocks of $g = 5$ or 6 consecutive beads relative to the overall charge asymmetry of the polyampholyte in the form of $\kappa \sim \sum_{\beta=1}^{N_p-g+1} [(\sum_{\alpha=\beta}^{\beta+g-1} \sigma_\alpha)^2 / (\sum_{\alpha=\beta}^{\beta+g-1} |\sigma_\alpha|) - (\sum_{\alpha=1}^{N_p} \sigma_\alpha)^2 / (\sum_{\alpha=1}^{N_p} |\sigma_\alpha|)]^2$ (refs. 13, 37). In contrast, $\text{SCD} \equiv \sum_{\alpha=2}^{N_p} \sum_{\beta=1}^{\alpha-1} \sigma_\alpha \sigma_\beta \sqrt{\alpha - \beta} / N_p$ takes into account nonlocal sequence charge pattern as it accords higher weights for sequence-nonlocal pairs of charges.¹⁴

Following several seminal studies,^{13,14,22,27} we consider $N_p = 50$ overall-neutral polyampholytes with $\sigma_\alpha = \pm 1$ (in units of the protonic charge) and $\sum_{\alpha=1}^{N_p} \sigma_\alpha = 0$. Substantiating a preliminary analysis,³⁷ we rigorously determine the joint distribution $P(\text{SCD}, \kappa)$ among all such sequences by first estimating the populated region in the (SCD, κ)-plane via a diversity-enhanced genetic algorithm³⁸ and then obtaining $P(\text{SCD}, \kappa)$ in the identified region using a Wang-Landau approach³⁹ (all $\text{SCD} < 0$;²⁴ see text and Fig. S1a of Supporting Information for details). The resulting heat map for $P(\text{SCD}, \kappa)$ in Fig. 1a exhibits a moderate correlation between $-\text{SCD}$ and κ (Pearson correlation coefficient $r = 0.684$).

Among these 50mers, we select for further analysis 26 sequences with a broad coverage in Fig. 1a and are illustrative of sequence variations of interest (Fig. 1b). Beside the 12 “sv” sequences as examples of the 30 original sv sequences¹³ are the 4 “as” sequences as controls for their $-\text{SCD}-\kappa$ anticorrelation opposing the overall positive correlation.³⁷ To probe the differential effects of sequence-local versus nonlocal charge patterns, we construct 4 “c κ ” sequences with diverse SCDs but essentially the same κ , and 4 “cSCD” sequences with diverse κ s but essentially the same SCD. We also consider sequences obs1 and ebs1 with odd and even numbers of charge blocks, respectively, to assess effects of like versus opposite charges at the two chain ends. These sequences and their κ and $-\text{SCD}$ values are listed in Table S1 and Fig. S1b of Supporting Information and marked in Fig. 1a. By focusing on this set of sequences with the same chain length, we address sequence charge patterns’ impact on the thermodynamics of polyampholytes. As such, further investigations of dynamic and other material properties,^{40–42} broader questions about sequence specificity for IDPs of different chain lengths,^{43,44} polyampholytes in high salt,⁴⁵ and for sequences containing short spatial range hydrophobic-like interactions^{46–50} and/or with high net charges^{51,52} are left to future studies.

Theories and computational models are available to address sequence-specific LLPS of polyampholytes (see, e.g., refs. 53–57, reviewed in ref. 58). Here we apply three complementary methods: analytical random phase approximation (RPA),^{53,54} field-theoretic simulation (FTS),^{28,56,59,60} and coarse-grained molecular dynamics (MD) with the “slab”

sampling method for phase equilibria⁶¹ (formulations described in Supporting Information), which have afforded numerous physical insights.^{7,27,30,48,62} Based on the same path-integral polymer model, FTS is more accurate than RPA in principle because it does not require an approximation like RPA and can be extended to tackle nonelectrostatic interactions.⁴⁸ Nonetheless, FTS is limited by finite resolution, simulation box size, and treatments of excluded volume.^{27,30} Compared to RPA and FTS, coarse-grained MD accounts better for structural and energetic features of IDPs^{47,49,63–65} but is computationally more costly. To focus on electrostatics, we adopt the “hard-core repulsion” MD model with no nonelectrostatic attraction.³⁷ The utility of combining the complementary advantages of RPA, FTS, and MD is illustrated by recent studies of the dielectric properties of condensates²⁹ and the effects of salt and ATP on condensed polyampholytic and polyelectrolytic biomolecules.⁵²

We employ all three methods for LLPS. R_g s and pairwise bead-bead contacts—which are not amenable to RPA currently—are computed by MD and the following FTS approach: In a multiple-chain system, the root-mean-square radius of gyration of the i th polymer $R_g^{(i)2} = \langle \sum_{\alpha=1}^{N_p} \sum_{\beta=1}^{N_p} (\mathbf{R}_{i,\alpha} - \mathbf{R}_{i,\beta})^2 \rangle / 2N_p^2 = \int d\mathbf{r} \int d\mathbf{r}' \langle \hat{\rho}_c^{(i)}(\mathbf{r}) \hat{\rho}_c^{(i)}(\mathbf{r}') \rangle (\mathbf{r} - \mathbf{r}')^2 / 2N_p^2$, where $\langle \dots \rangle$ denotes Boltzmann averaging, $\mathbf{R}_{i,\alpha}$ is the position of the α th bead along the chain, and $\hat{\rho}_c^{(i)}(\mathbf{r}) \equiv \sum_{\alpha=1}^{N_p} \delta(\mathbf{r} - \mathbf{R}_{i,\alpha})$ is the position (\mathbf{r})-dependent bead center density. Since the correlation function $G^{(i)}(|\mathbf{r} - \mathbf{r}'|) = \langle \hat{\rho}_c^{(i)}(\mathbf{r}) \hat{\rho}_c^{(i)}(\mathbf{r}') \rangle$ that depends on the relative distance $|\mathbf{r} - \mathbf{r}'|$ is amenable to FTS,³⁰

$$R_g^{(i)2} = \frac{V}{2N_p^2} \int d\mathbf{r} G^{(i)}(|\mathbf{r}|) |\mathbf{r}|^2, \quad (1)$$

where system volume $V = \int d\mathbf{r}$, can now be computed by FTS. Similarly, with a generalized correlation $G_{\alpha,\beta}^{(i),(j)}(|\mathbf{r}|)$ between the α th bead of the i th chain and the β th bead of the j th chain,

$$\omega_{\alpha,\beta}^{i,j} = V \int_0^{2b} d\mathbf{r} G_{\alpha,\beta}^{i,j}(|\mathbf{r}|) \quad (2)$$

is seen as the frequency of contact between the two beads, i.e., when their centers are within a small distance (chosen here as $2b$ where b is the reference bond length between sequentially consecutive beads). Thus, through appropriate choices of i and j , intrachain contacts of an isolated chain as well as intrachain and interchain contacts in the condensed phase (Fig. 1c) can be computed by FTS via $G_{\alpha,\beta}^{(i),(j)}(|\mathbf{r}|)$. A derivation of this formulation based on the general FTS approach^{56,66–68} is provided in the Supporting Information.

As examples, Fig. 1d,e show the RPA, FTS, and MD phase diagrams for six sequences. Phase diagrams for all 26 sequences in Fig. 1b are provided in Fig. S2 of the Supporting Information. To facilitate comparisons, temperatures are given as reduced temperature $T^* \equiv b/l_B$ where l_B is Bjerrum length. Because of the models’ different effective energy scales arising from various approximations and treatments of excluded volume, the critical temperatures, T_{cr}^* s, predicted by RPA, FTS, and MD can be substantially different for the

same sequence (Fig. S1b in Supporting Information). Nonetheless, the variation in T_{cr}^* predicted by the models are well correlated (Fig. 1f, Pearson correlation coefficients $r \gtrsim 0.95$), indicating that the models are capturing essentially the same sequence-dependent trend of LLPS propensity. As to the relationship between T_{cr}^* and T^* -dependent root-mean-square isolated-chain R_{g} , a T^* sufficiently high for a large sequence-dependent variation in R_{g} is chosen for each of the models in Fig. 1g. Consistent with an earlier study on sv sequences,²² R_{g} s of isolated polyampholytes are well correlated with their T_{cr}^* s in all three models (Fig. 1g). Notably, however, there is an appreciable $R_{\text{g}}-T_{\text{cr}}^*$ scatter in the MD model involving the cSCD, $c\kappa$, obs1, and ebs1 sequences which as a group is less conformative to the moderate $-\text{SCD}-\kappa$ correlation than the sv sequences (Fig. 1a).

The impact of sequence-local versus nonlocal charge pattern on R_{g} and T_{cr}^* is assessed by comparing the extent to which they are (anti)correlated with κ and SCD (Fig. 2). R_{g} depends on T^* . Since the charge-pattern-dependent variation in R_{g} among sequences with moderate to high $-\text{SCD}$ values is small at low T^* as they adopt conformations with similarly high compactness, two T^* s are chosen for each of the FTS and MD models in Fig. 2a,b,e,f with the higher T^* producing ample R_{g} variations across the entire ranges of $-\text{SCD}$ and κ . Corresponding R_{g} data for additional T^* s are provided in Fig. S3 of Supporting Information.

It is clear from Fig. 2a,b,e,f that R_{g} anticorrelates significantly better with $-\text{SCD}$ than κ . For the sv sequences, R_{g} anticorrelates reasonably well with both $-\text{SCD}$ and κ . Indeed, the significant $\kappa-R_{\text{g}}$ scatter seen in both FTS and MD (Fig. 2e,f) involves the as, cSCD, and $c\kappa$ sequences we introduced. Despite the large variations in κ among the as and cSCD sequences, their R_{g} s are very similar. For the $c\kappa$ sequences, despite their essentially identical κ , their R_{g} s are very different. By comparison, the excellent $-\text{SCD}-R_{\text{g}}$ anticorrelation is maintained when challenged by these sequences (Fig. 1a,b). In this light, the good $\kappa-R_{\text{g}}$ anticorrelation observed previously for the sv sequences¹³ is largely attributable to the good correlation between the κ values of this particular set of sv sequences and their $-\text{SCD}$ s.

In contrast to κ and SCD's clearly different performance for R_{g} (which is the original target of both parameters^{13,14}, neither of these parameters was derived originally for multiple-chain properties), their correlations with T_{cr}^* are more comparable (Fig. 2c,d,g,h). Unlike the excellent $-\text{SCD}-R_{\text{g}}$ anticorrelation, both the $-\text{SCD}-T_{\text{cr}}^*$ and $\kappa-T_{\text{cr}}^*$ correlations are good but not excellent. While $-\text{SCD}$ is better than κ with T_{cr}^* for RPA and FTS (Fig. 2c,g), κ is slightly better for MD (Fig. 2d,h). Notably, for all three models—RPA, FTS, and MD—the variation in T_{cr}^* is larger among the $c\kappa$ than among the cSCD sequences.

The origin of the performances of $-\text{SCD}$ and κ for R_{g} is explored by first considering how R_{g} is related to intrachain contacts for a homopolymer with favorable short-spatial-range interactions (model described in Supporting Information). In this baseline model, R_{g} s conditioned upon pairwise α, β contacts (Fig. 3a, top map, upper triangle) indicate that more nonlocal (higher-order) contacts lead to smaller R_{g} . Sequence-local and nonlocal

interactions thus have different implications for R_g . This basic observation offers a semi-quantitative rationalization for SCD’s better performance with regard to R_g because, as entailed by the original approximate analytical theory,¹⁴ nonlocal electrostatic interactions (larger $|\alpha - \beta|$) are more heavily weighted in SCD than local interactions (smaller $|\alpha - \beta|$).

Additional information is provided by contact patterns (Fig. 3a–d). The intrachain contact frequencies $P_{\alpha,\beta}^{[i]}$ and $P_{\alpha,\beta}^{[c]}$ are the average numbers of contacts between the α th and β th beads, respectively, of an isolated chain (at infinite dilution) and a chain in the condensed phase, whereas the interchain $C_{\alpha,\beta}^{[c]}$ is the average number of contacts between the α th bead of one chain and the β th bead of another chain. By definition, $P_{\alpha,\beta}^{[i]} = P_{\beta,\alpha}^{[i]}$, $P_{\alpha,\beta}^{[c]} = P_{\beta,\alpha}^{[c]}$, and $C_{\alpha,\beta}^{[c]} = C_{\beta,\alpha}^{[c]}$. For the baseline homopolymer, the isolated-chain $P_{\alpha,\beta}^{[i]}$ ’s pattern is typical of Gaussian or self avoiding walk conformations, with substantially lower frequencies for higher order contacts³² (Fig. 3a, top map, lower triangle). The condensed-phase intrachain pattern (Fig. 3a, bottom map, lower triangle) shares a similar trend but with less variation in contact frequency (cf. heat map scales for $-\ln P_{\alpha,\beta}^{[i]}$ and $-\ln P_{\alpha,\beta}^{[c]}$ in Fig. 3a). In contrast, the interchain $C_{\alpha,\beta}^{[c]}$ is quite insensitive to α, β except it is slightly higher when either α, β , or both, are at or near the chain ends (Fig. 3a, bottom map, upper triangle).

Polyampholyte contact data are illustrated here by an example sequence. The MD (Fig. 3b) and FTS (Fig. 3c) patterns are quite well correlated, their differences likely arise from the differing treatments of excluded volume in the two approaches.^{27,30} Data for the other 25 sequences in Fig. 1b are in Fig. S4 of Supporting Information. In Fig. 3b, the R_g map exhibits sequence-specific features as well as a contact-order dependence (top map, upper triangle) indicating differential sequence-local versus nonlocal effects on R_g . Similar to the homopolymer (Fig. 3a), the intrachain pattern of an isolated polyampholyte (Fig. 3b,c top map, lower triangle) is similar to that of a polyampholyte in the condensed phase (Fig. 3b,c bottom map, lower triangle). Unlike the homopolymer, the isolated-chain intrachain pattern (Fig. 3b,c top map, lower triangle) is similar also to the condensed-phase interchain pattern (Fig. 3b,c bottom map, upper triangle). This feature, which is echoed by the comparison in Fig. 3e below, applies to the other 25 sequences as well.

Averages of $P_{\alpha,\beta}^{[i]}$, $P_{\alpha,\beta}^{[c]}$, or $C_{\alpha,\beta}^{[c]}$ for a given $|\alpha - \beta|$ are illustrated here using the homopolymer model and the example sequence (Fig. 3d,e). Similar salient features are exhibited by the other 25 sequences (Fig. S5 of Supporting Information). Condensed-phase interchain $C_{\alpha,\beta}^{[c]}$ is least sensitive to $|\alpha - \beta|$ for the homopolymer (Fig. 3d) and for polyampholytes (Fig. 3e). Notably, the polyampholyte interchain $C_{\alpha,\beta}^{[c]}$ (orange curve) is closer to the isolated-chain intrachain $P_{\alpha,\beta}^{[i]}$ (green curve) than to the condensed-phase intrachain $P_{\alpha,\beta}^{[c]}$ (blue curve). The root-mean-square distance $R_{\alpha\beta}$ between beads α and β is highly sensitive to sequence¹³ and temperature for an isolated polyampholyte (Fig. 3f) as its R_g decreases at low T^* . In contrast, Fig. 3g shows that $R_{\alpha\beta}$ depends only weakly on T^* . Depending on the sequence, R_g can increase or decrease slightly with T^* (Fig. S6 of Supporting

Information). As in homopolymer melts,⁶⁹ condensed-phase polyampholytes adopt open, essentially Gaussian-like conformations ($R_{\alpha\beta}/\sqrt{|\alpha-\beta|} \sim \text{constant}$ except for small $|\alpha-\beta|$ in Fig. 3g), a phenomenon also seen in recent simulations of biomolecular condensates.⁷⁰⁻⁷³

To gain further insights, we compare sequence-specific contact patterns such as those in Fig. 3b by the following symmetrized form of the Kullback-Leibler divergence⁷⁴ between contact frequencies $\{C_{\alpha\beta}^{(s)}\}$ and $\{C_{\alpha\beta}^{(s')}\}$ (contact maps) of a pair of sequences s, s' :

$$D_{s,s'} = \sum_{\alpha=1}^{N_p-d_m} \sum_{\beta=\alpha+d_m}^{N_p} \left[c_{\alpha\beta}^{(s)} - c_{\alpha\beta}^{(s')} \right] \ln \left[c_{\alpha\beta}^{(s)} / c_{\alpha\beta}^{(s')} \right], \quad (3)$$

where d_m serves to exclude local contacts—which are often highly populated—from overwhelming the contact pattern’s quantitative characterization, and $c_{\alpha\beta}^{(s)} \equiv C_{\alpha\beta}^{(s)} / \sum_{\alpha'=1}^{N_p-d_m} \sum_{\beta'=\alpha'+d_m}^{N_p} C_{\alpha'\beta'}^{(s)}$ are normalized frequencies. The comparisons of $P_{\alpha,\beta}^{[i]}$ with $P_{\alpha,\beta}^{[c]}$ (Fig. 4a) and with $C_{\alpha,\beta}^{[c]}$ (Fig. 4b) entail significant scatter. Nonetheless, the relatively low $D_{s,s'}$ values for $s = s'$ (black circles) in Fig. 4b is consistent with the impression from Fig. 3b,c that the patterns of isolated-chain intrachain and condensed-phase interchain contacts are similar for a given polyampholyte. This trend prevails for several other d_m values and another isolated-chain T_{iso}^* (Fig. S7 of Supporting Information), underpinning correlations between sequence-dependent isolated-chain and condensed-phase properties.

The relationship between isolated-chain and condensed-phase properties is further elucidated by examining the total number of contacts made by a polyampholyte. Whereas the number of intrachain contacts of an isolated chain correlates poorly with that of a condensed-phase chain (Fig. 4c) because of their significantly different R_g s (see above), an excellent correlation is seen between the number of intrachain contacts of an isolated chain with the number of interchain contacts in the condensed phase (Fig. 4d), echoed by the excellent correlation between isolated-chain and condensed-phase potential energies (Fig. 4e). Similar trends are seen for other values of T_{iso}^* (Fig. S8 and Fig. S9a of Supporting Information). T_{cr}^* anticorrelates reasonably well with isolated-chain potential energy $E^{[i]}$ (Fig. 4f), which expectedly correlates with the number of interchain contacts (Fig. S9b in Supporting Information). Notably, $E^{[i]}$, in turn, anticorrelates quite well with κ (Fig. 4h) but not so well with $-\text{SCD}$ (Fig. 4g), indicating that in some situations κ can be a better predictor of LLPS propensity, suggesting that differential effects of sequence-local versus nonlocal interactions may be less prominent for LLPS than for isolated-chain R_g . This understanding is underscored by the fitting coefficients c_κ for κ and c_{SCD} for SCD in Fig. 4i,j indicating that variation in R_g can be accounted for essentially entirely by SCD ($c_\kappa \approx 0$) but variation in T_{cr}^* is rationalized approximately equally by κ and SCD ($c_\kappa \approx c_{\text{SCD}}$). κ is not a good general predictor for R_g though κ correlates well with $E^{[i]}$ because R_g is not determined solely by $E^{[i]}$. For instance, two chains each constrained

by one contact with the same energy but different contact orders can have very different R_g s.

To recapitulate, many IDPs can exist in dilute and condensed phases serving different biological functions. Single-chain IDP R_g s in dilute solutions, readily accessible experimentally,⁷⁵ have been used to benchmark MD potentials for sequence-dependent IDP properties.^{76,77} Isolated-chain contact maps,⁷⁸ related topological constructs such as SCDM⁷⁹ and energy maps,⁸⁰ and their relations with condensed-phase interchain contact maps^{11,65} have proven useful in recent computational analyses. For instance, isolated-chain intrachain and condensed-phase interchain contacts are similar for heterochromatin protein 1 paralogs⁸¹ and EWS sequences⁷² but not the TDP-43 C-terminal domain.⁸² Here, our findings indicate a fundamental divergence in the differential impact of local versus nonlocal sequence patterns on isolated, single-chain and condensed-phase multiple-chain properties. The differential impact is prominent for isolated-chain conformational dimensions due to chain connectivity.³² It is substantially less for LLPS propensity because the multiple-chain nature of condensed-phase interactions dampens—though not entirely abolish—the effects of contour separations between residues along a single connected sequence due to the immense number of configurations in which residues from different chains may interact. This is a fundamental factor in the dilute/condensed-phase relationship of IDPs that needs to be taken into account when devising improved sequence pattern parameters for the characterization of physical and functional IDP molecular features.^{16,83} Inasmuch as such parameters’ aim is instant estimation of LLPS propensity, theoretical quantities that can be numerically computed efficiently—such as the T_{cr}^* predicted by RPA-related theories⁴⁸—may just serve the purpose practically even if they are not closed-form mathematical expressions.

Supporting Information

Methodological and formulational details, supporting table, and supporting figures

Acknowledgements. This work was supported by Canadian Institutes of Health Research (CIHR) grant NJT-155930 and Natural Sciences and Engineering Research Council of Canada (NSERC) grant RGPIN-2018-04351 to H.S.C. We are grateful for the computational resources provided generously by the Digital Research Alliance of Canada.

Figures (Main Text)

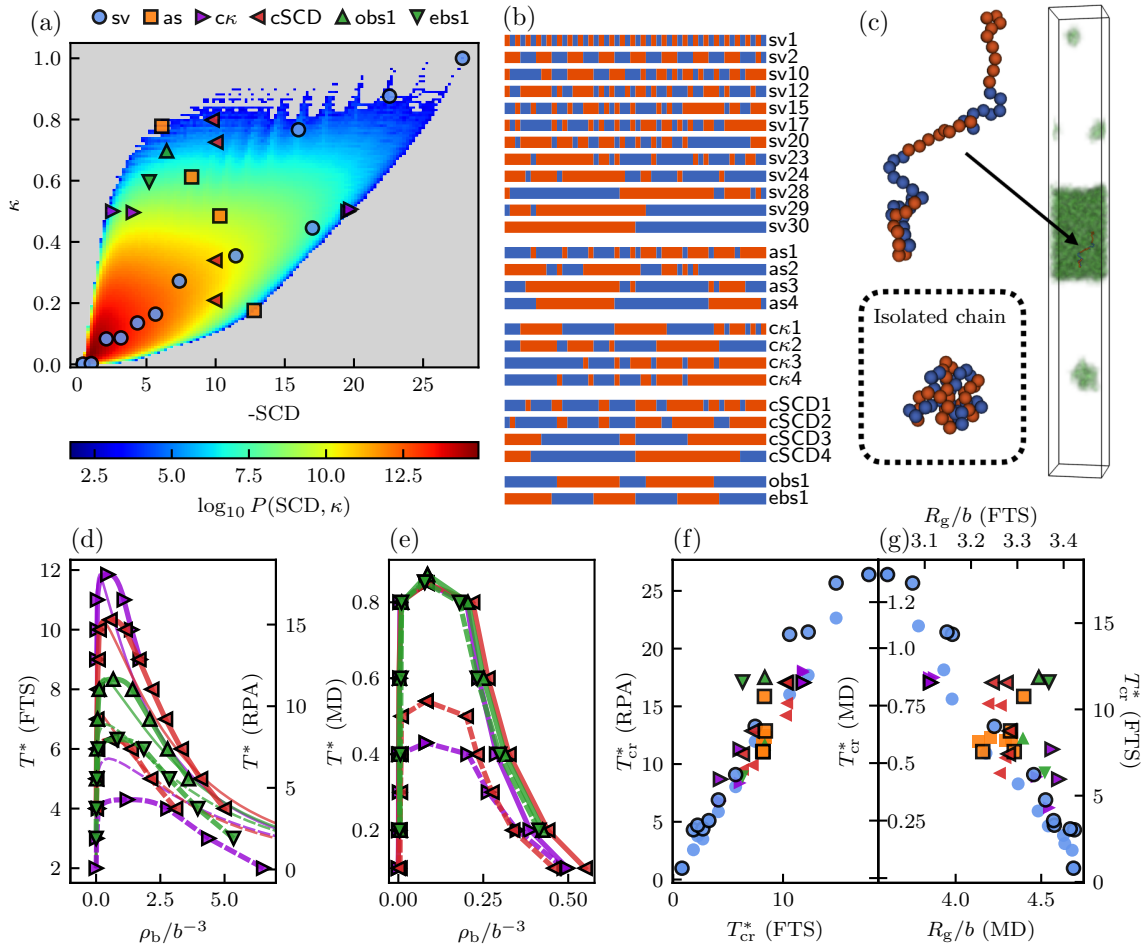


Figure 1: Polyampholytes with representative variations in local and nonlocal sequence charge patterns. (a) The SCD- κ sequence-space population distribution of 50-bead polyampholytes is depicted by a heat map (bottom scale, region with zero population is in gray), wherein the 26 sequences studied (b) are marked by symbols (a, top). (b) The positive (blue) and negative (red) charge patterns of these sequences. (c) Coarse-grained MD snapshots showing a conformation in the condensed phase (top) and an isolated conformation (dotted box). (d,e) Phase diagrams in RPA (thin continuous curves), FTS (symbols) (d), and MD (symbols) (e) for sequences κ 1, κ 4, cSCD1, cSCD4, ebs1, and obs1. Thick solid and dashed lines connecting symbols in (d) and (e) are merely guides for the eye. (f) T_{cr}^* s of all 26 sequences predicted by different theories. The $T_{cr}^* - T_{cr}^*$ Pearson correlation coefficients for RPA-FTS, RPA-MD, and FTS-MD are, respectively, $r = 0.997$, 0.945 , and 0.948 . Data symbols in (f) and (g) involving MD are identified by black edges. (g) Correlation between T_{cr}^* and R_g in FTS (at $T^* = 20$, $r = -0.954$) or in MD (at $T^* = 10$, $r = -0.842$). A complete list of T_{cr}^* s and phase diagrams for all sequences in (b) predicted by the RPA, FTS, and MD models are provided in Figs. S1 and S2 of the Supporting Information.

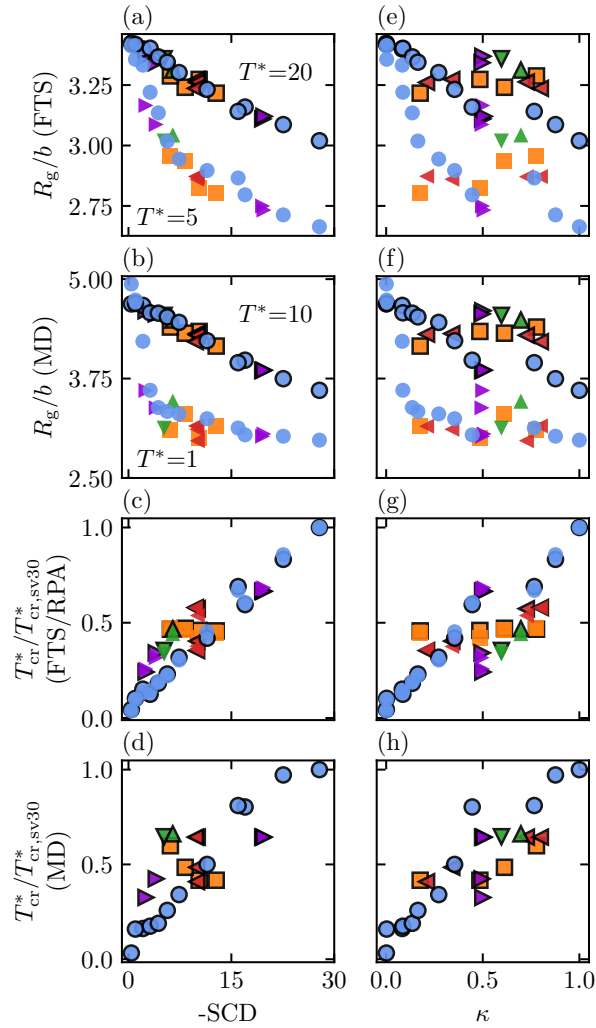


Figure 2: SCD and κ as predictors for isolated-chain R_g and multiple-chain LLPS critical temperature T_{cr}^* . Symbols for polyampholytes are those in Fig. 1a. (a,b,e,f) R_g computed by FTS (a,e) and MD (b,f) versus $-\text{SCD}$ (left) or κ (right). Symbols with and without black edges are for different temperatures (T^* s). $-\text{SCD}-R_g$ correlation coefficients are $r = -0.983$ for FTS at $T^* = 20$ (a) and $r = -0.991$ for MD at $T^* = 10$ (b), the corresponding $\kappa-R_g$ values are $r = -0.665$ (e) and -0.627 (f). (c,d,g,h) T_{cr}^* in FTS, RPA [depicted, respectively, in (c,g) by symbols with and without black edges] and MD (d,h) are plotted in units of the T_{cr}^* for sequence sv30 ($T_{\text{cr,sv30}}^*$). The $-\text{SCD}-T_{\text{cr}}^*$ r values are: 0.943 for RPA, 0.932 for FTS (c), and 0.834 for MD (d). The corresponding $\kappa-T_{\text{cr}}^*$ values are $r = 0.827$ for RPA, 0.841 for FTS (g), and 0.886 for MD (h).

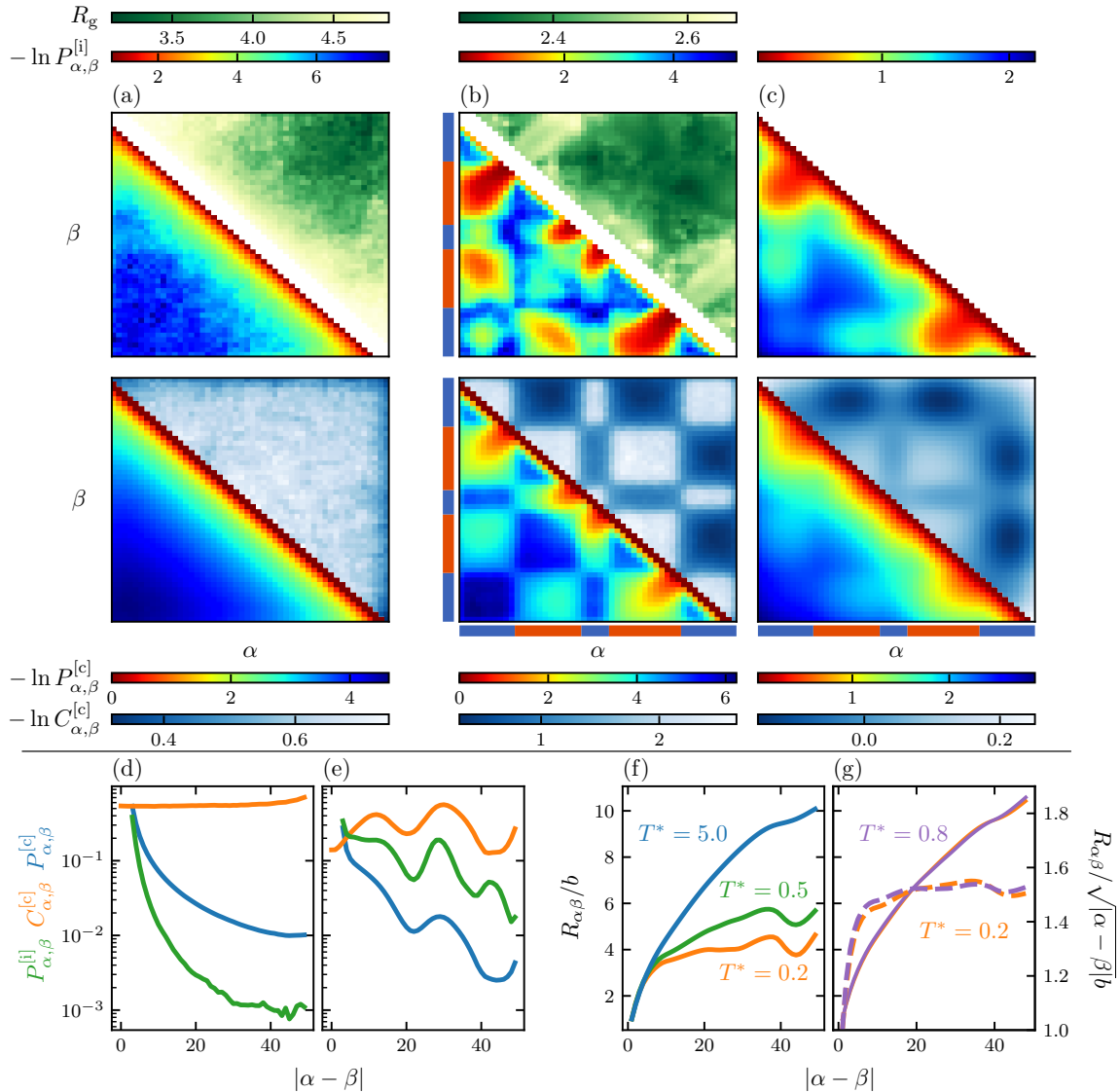


Figure 3: Contact patterns of polyampholytes as an isolated chain versus in the phase-separated condensed phase. (a–c) Top heat maps (color scales above) show isolated-chain contact frequencies (lower triangle) and R_g conditional upon intrachain i, j contacts (upper triangle); bottom maps (color scales below) show condensed-phase intrachain (lower triangle) and interchain contact frequencies (upper triangle); $\alpha, \beta = 1, 2, \dots, 50$ are bead labels along the chain. Contact frequencies $P_{\alpha, \beta}^{[i]}$, $P_{\alpha, \beta}^{[c]}$, and $C_{\alpha, \beta}^{[c]}$ are defined in the text. Data are shown for (a) the baseline homopolymer (MD, $T^* = 2.0$) and (b) the sequence obs1 (MD, $T^* = 0.2$). The charge pattern of obs1 (as in Fig. 1b) is depicted along the axes in (b). (c) Corresponding FTS contact maps for obs1 at $T^* = 3.0$. (d, e) Contact frequencies (color coded as indicated) in MD as functions of contact order $|\alpha - \beta|$ for (d) the baseline homopolymer ($T^* = 2.0$) and (e) obs1 ($T^* = 0.2$). (f, g) MD-simulated obs1 intrachain root-mean-square distance $R_{\alpha\beta}$ (solid curves, left vertical scale) at select temperatures for an isolated chain (f) and in the condensed phase (g); to facilitate analysis (see text), $R_{\alpha\beta}/\sqrt{|\alpha - \beta|}$ plots (dashed curves, right vertical scale) are also provided in (g).

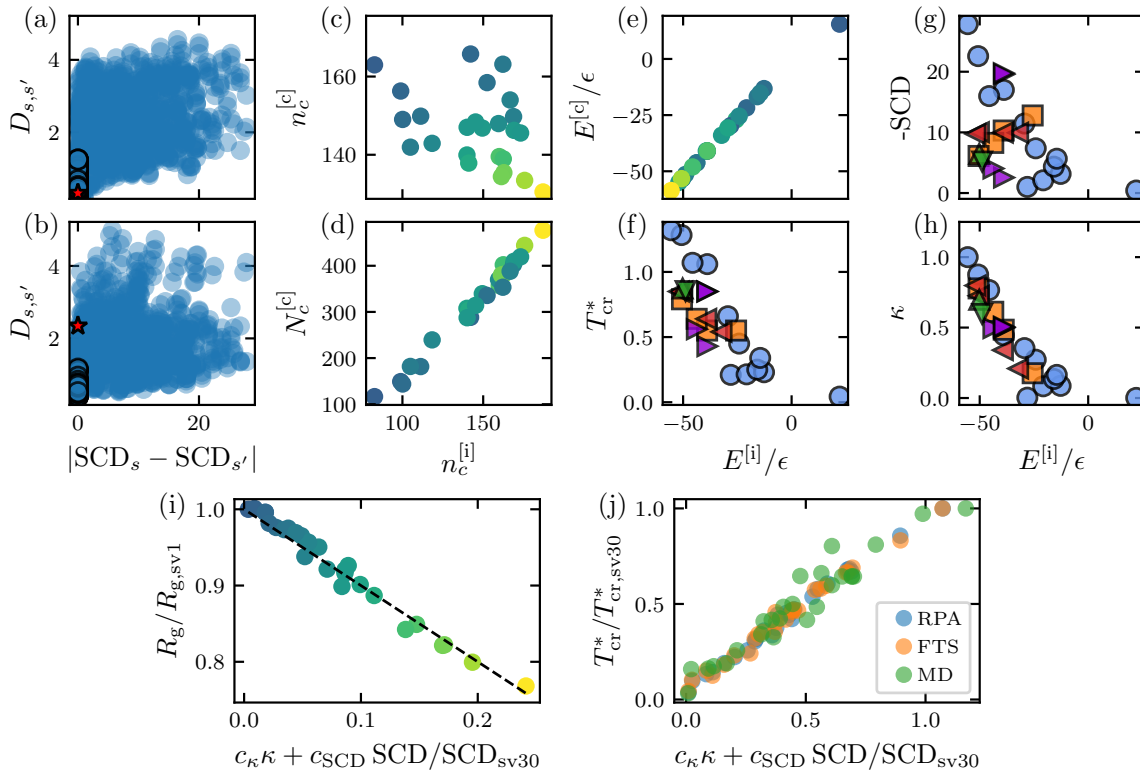


Figure 4: Impact of local versus nonlocal sequence charge pattern on polyampholyte contacts and interaction energies in the MD model. (a,b) $D_{s,s'}$ is symmetrized Kullback-Leibler divergence between the normalized $|\alpha - \beta| \geq 4$ contact frequencies of sequences s and s' (see text). The scatter plots show $D_{s,s'}$ versus s - s' SCD difference. Each datapoint (translucent blue circle) provides the $D_{s,s'}$ between the intrachain contacts of an isolated chain (s) and (a) the intrachain or (b) interchain contacts of a condensed-phase chain (s') where $s, s' = 25$ of the sequences in Fig. 1b (all except sv1), with $T_{\text{iso}}^* = 0.2$, $0.1 \leq T_{\text{cond}}^* \leq 0.3$, and $s = s'$ datapoints as black circles. Red stars are $D_{s,s'}$ values for the baseline homopolymer at $T^* = 2.0$. (c,d) Scatter plots of number of intrachain contacts of isolated chains $n_c^{[i]}$ with number of (c) intrachain contacts $n_c^{[c]}$ ($r = -0.396$) or (d) interchain contacts $N_c^{[c]}$ in the condensed phase ($r = 0.992$) for the 25 sequences analyzed in (a,b). (e-h) Scatter plots of isolated-chain potential energy $E^{[i]}$ (in units of ϵ , for all 26 sequences) with (e) condensed-phase potential energy $E^{[c]}$ ($r = 0.998$), (f) T_{cr}^* ($r = -0.808$), (g) SCD ($r = 0.505$), or (h) κ ($r = -0.855$). Datapoints for different sequences in (c-e,i) are color-coded for SCD, with lighter color corresponding to larger $-\text{SCD}$ (as in Figs. S8 and S9). Symbols in (f-h) corresponds to those in Fig. 1a. All quantities in (c-h) are computed for $T^* = 0.2$ except a lower $T^* = 0.04$ sufficient for LLPS of sv1 is used to obtain $E^{[c]}$ for sv1 in (e). (i,j) Best-fit linear combinations of κ and SCD as predictors for (i) R_g (in units of R_g of sv1, $R_{g,sv1}$, at $T^* = 10$) and (j) T_{cr}^* for all sequences in Fig. 1a. (i) The dashed line is $R_g = 1 - (c_\kappa \kappa + c_{\text{SCD}} \text{SCD}/\text{SCD}_{\text{sv30}})$ with $c_\kappa = -0.0017$, $c_{\text{SCD}} = 0.243$ ($r = -0.991$), and SCD_{sv30} is the SCD of sv30. (j) The best-fit parameters are $a_\kappa = 0.39$, $c_{\text{SCD}} = 0.68$ for RPA ($r = 0.996$), $c_\kappa = 0.42$, $c_{\text{SCD}} = 0.65$ for FTS ($r = 0.994$), and $c_\kappa = 0.63$, $c_{\text{SCD}} = 0.54$ for MD ($r = 0.962$).

July 4, 2024

Supporting Information

for

Differential Effects of Sequence-Local versus Nonlocal Charge Patterns on Phase Separation and Conformational Dimensions of Polyampholytes as Model Intrinsically Disordered Proteins

Tanmoy PAL,^{1,†} Jonas WESSÉN,^{1,†} Suman DAS,^{1,2,†} and Hue Sun CHAN^{1,*}

¹Department of Biochemistry, University of Toronto, Toronto, Ontario M5S 1A8, Canada

²Department of Chemistry, Gandhi Institute of Technology and Management,
Visakhapatnam, Andhra Pradesh 530045, India

†Contributed equally.

*Correspondence information:

Hue Sun CHAN. E-mail: huesun.chan@utoronto.ca

Tel: (416)978-2697; Fax: (416)978-8548

Department of Biochemistry, University of Toronto, Medical Sciences Building – 5th Fl.,
1 King's College Circle, Toronto, Ontario M5S 1A8, Canada.

Methodological and Formulation Details

Estimating the sequence-space distribution $P(\text{SCD}, \kappa)$

As outlined in the maintext, we investigate the relationship between the SCD and κ parameters and its ramifications on isolated-chain and condensed-phase conformational properties by first calculating their distribution $P(\text{SCD}, \kappa)$ for electrically overall neutral 50mer polyampholytes (sequences with 50 beads). Following convention in an earlier work that used lysine (K) for the positively charged (+1) and glutamic acid (E) for the negatively charged (-1) monomers/residues along the chain sequence,¹³ we refer to the sequences under consideration as K/E sequence in the following discussion, keeping in mind, however, that K and E here refer only to +1 and -1 polymer beads with no sidechain structure, as in several previous simplified models.^{14,22,27,37} Values for κ are computed in the present work using the $\kappa = (\kappa_5 + \kappa_6)/2$ expression defined in ref. 37.

The $P(\text{SCD}, \kappa)$ distribution is defined in such a way that $P(\text{SCD}', \kappa') \Delta\text{SCD} \Delta\kappa$ is the number of possible sequences with (SCD, κ) values in a small region $\Delta\text{SCD} \Delta\kappa$ (two-dimensional bin) in the vicinity of (SCD', κ') . We compute $P(\text{SCD}, \kappa)$ using the Wang-Landau (WL) algorithm,³⁹ which is a highly efficient flat-histogram method for estimating multi-peaked densities of states. However, before setting up the WL algorithm, prior knowledge about the the mathematically possible (κ, SCD) combinations is required since the WL algorithm relies on checking that all (κ, SCD) bins are evenly sampled.

To find the region in the (SCD, κ) -plane that can support 50mer K/E sequences, we utilize a genetic algorithm (GA) that is capable of scanning the space of sequences efficiently. Specifically, this GA takes an input target point $(\text{SCD}_{\text{target}}, \kappa_{\text{target}})$ in sequence space and attempts to generate a new sequence $\{\sigma_\alpha\}$ ($\alpha = 1, 2, \dots, N$, where the chain length $N = 50$) with (SCD, κ) that maximizes the fitness function

$$f(\{\sigma_\alpha\}) = -(\kappa - \kappa_{\text{target}})^2 - 0.001(\text{SCD} - \text{SCD}_{\text{target}})^2. \quad (\text{S1})$$

For a given target $(\text{SCD}_{\text{target}}, \kappa_{\text{target}})$, the algorithm proceeds as follows:

1. Generate an initial “population” of $n_{\text{population}} = 100$ random electrically neutral K/E sequences (each with 25 K and 25 E).
2. Each sequence in the population is used to generate $n_{\text{offspring}} = 50$ “offspring” sequences. Every offspring sequence is generated from its parent sequence using one of the following prescriptions:
 - *Single flip (50%)*: A randomly selected pair of K/E residues are interchanged.
 - *Cluster move (45%)*: A randomly selected block of same-charge residues is moved one step (either left or right chosen at random), e.g., ...EEEEK... \rightarrow ...KEEEEK... . As such, this is a special case of single flip. It serves to enhance sampling of blocky sequences.

- *New sequence (5%)*: An entirely new electrically neutral sequence with no relation to the parent sequence is randomly generated.

The three prescriptions are chosen at random with probabilities provided in parentheses above. We do not use crossover to generate offspring sequences (i.e. where multiple parent sequences are combined to generate offspring) as initial exploratory runs did not reveal any major advantage when using crossover.

3. We next select $n_{\text{survivors}} = 30$ out the $n_{\text{population}} \cdot n_{\text{offspring}}$ offspring sequences using a diversity enhanced survivor selection algorithm. First, we evaluate the fitness f_i of each offspring sequence $\{\sigma_\alpha^{(i)}\}$, with $i = 1, \dots, n_{\text{population}} \cdot n_{\text{offspring}}$, according to Eq. (S1), and select the sequence corresponding to the highest (least negative) f_i as the first survivor. The fitness of the remaining sequences $\{\sigma_\alpha^{(j \neq i)}\}$ are then modified as $f_j \rightarrow f_j - e^{-10d_{ij}}$ where $d_{ij} = \sum_{\alpha=1}^N (\sigma_\alpha^{(i)} - \sigma_\alpha^{(j)})^2 / 4N$. This step punishes sequences that are identical or near-identical to the first selected survivor. The next survivor i' is then selected based on the updated fitnesses and the remaining sequences acquires new punishments depending on their similarity with i' . This procedure is repeated until $n_{\text{survivors}}$ have been selected.
4. The survivors now constitute the population of the next generation and steps 2–3 are iterated until either a sequence with $f_i \geq -10^{-5}$ has been found or the 10th generation of iterations is reached.

The diversity enhanced survivor selection procedure prevents the algorithm from being trapped in the vicinity of a local fitness maximum since sequences are selected both according to having a high fitness and being dissimilar to other sequences with high fitness. The method was introduced to scan for experimentally viable parameter regions in extensions of the Standard Model in particle physics,³⁸ but the survivor selection procedure was not outlined in full detail in ref. 38.

We coarse-grain the (SCD, κ)-plane into 120×120 bins that cover the rectangular region $\text{SCD} \in [\text{SCD}_{\text{sv30}}, 0]$ (i.e., $-\text{SCD} \in [0, -\text{SCD}_{\text{sv30}}]$), $\kappa \in [0, 1]$, where SCD_{sv30} is the SCD value of the diblock sequence sv30 in ref. 13. The bin spanning the area $[-\text{SCD}_i, -\text{SCD}_i + \Delta\text{SCD}]$ and $[\kappa_j, \kappa_j + \Delta\kappa]$ is indexed by (i, j) (with $i, j = 1, \dots, 120$). The GA is first run for targets $(\text{SCD}_{\text{target}}, \kappa_{\text{target}})$ on the sites of an evenly spaced 7×7 grid (marked by white dots in the left panel of Fig. S1a). Every new bin visited during the scan is recorded and the associated sequence is stored. With the exception of the first target iteration, the above step 1 of the GA is modified such that the initial population is generated as offspring of the previously stored sequence with nearest SCD and κ to the target values instead of being randomly generated. The initial grid scan gives a rough estimate of (SCD, κ) region populated by sequences. Next, we iteratively run the GA for unvisited target bins adjacent to previously visited bins to map out the boundary of the region. Fig. S1a shows in the left panel the result of the GA scan, where bins for which a sequence was found are shown in black. White bins indicate target bins for which no sequence was found by the GA. For a few target bins,

the GA was not able to find a sequence but the subsequent WL scan (described below) revealed sequences populating these bins. These mislabelled bins are shown in red in the left panel of Fig. S1a.

The goal of the WL algorithm is to calculate the quantity $g_{i,j}$ representing the number of sequences with SCD and κ in bin (i, j) . To avoid numerical errors associated with large numbers, we (as is customary) formulate the algorithm in terms of $\ln(g_{i,j})$ rather than $g_{i,j}$. Another central quantity in the WL algorithm is the histogram $h_{i,j}$ over the number of visits in bin (i, j) . The WL algorithm operates as follows:

1. Initialize $h_{i,j} = \ln(g_{i,j}) = 0$ for all (i, j) and set the update factor $f = 1$.
2. Generate $n = 100$ random electrically neutral 50mer K/E sequences, $\{\sigma_\alpha^{(a)}\}$, $a = 1, \dots, n$, $\alpha = 1, 2, \dots, N$, and compute their associated SCD and κ values.

3. Perform the updates

$$\begin{aligned} h_{i,j} &\rightarrow h_{i,j} + 1, \\ \ln(g_{i,j}) &\rightarrow \ln(g_{i,j}) + f, \end{aligned} \tag{S2}$$

for the bin (i, j) associated with each sequence.

4. Check if $h_{i,j}$ is sufficiently flat. In this work, $h_{i,j}$ is deemed flat if

$$\frac{\langle h^2 \rangle - \langle h \rangle^2}{\langle h \rangle^2} < 0.5, \tag{S3}$$

where the averages are taken only over bins known to be populated by sequences. If the flatness condition is satisfied we reset $h_{i,j} = 0$ for all i, j and update f as $f \rightarrow f/2$.

5. Propose an update for every sequence $\{\sigma_\alpha^{(a)}\}$. The updates and their associated probabilities used in this work are

- *Single flip (80%)*: Flip the charges of a randomly selected pair of oppositely charged residues.
- *Multiple flips (20%)*: Perform n_{flip} single flips, where n_{flip} is a uniformly distributed random integer between 2 and 10.

Compute SCD and κ for all proposed sequences $\{\sigma_\alpha^{(a')}\}$ and accept the updates with probabilities

$$P_{\text{acc}} \left(\{\sigma_\alpha^{(a)}\} \rightarrow \{\sigma_\alpha^{(a')}\} \right) = \max \left(1, \frac{g_{i,j}}{g_{i',j'}} \right), \tag{S4}$$

where (i, j) and (i', j') refer to the bins associated with $\{\sigma_\alpha^{(a)}\}$ and $\{\sigma_\alpha^{(a')}\}$, respectively. If a (SCD, κ) combination is encountered for which the associated bin (i, j) was estimated by the GA as empty, the bin is re-labelled as non-empty and kept in all subsequent WL iterations.

6. Repeat steps 3–5 until 25 WL “levels” have been completed, i.e., until $h_{i,j}$ is flat with $f = 2^{-24}$.
7. Re-weight $g_{i,j} \rightarrow g_{i,j}/g_{sv30}$ where g_{sv30} is the value of $g_{i,j}$ for the bin associated with the di-block sequence sv30. This step accounts for the double counting associated with reversed sequences but relies on the discretization being sufficiently fine such that g_{sv30} only received contributions from sv30 and its reverse.

Our version of the WL algorithm differs from more standard implementations^{84,85} since $n = 100$ instantiations, rather than $n = 1$, of the system are evolved while modifying the same $g_{i,j}$ and $h_{i,j}$. As such, our setup shares characteristics with the replica-exchange Wang-Landau method,⁸⁶ although we do not e.g., constrain the individual sequences to subregions of the (SCD, κ)-plane. We observe a dramatic decrease in computation time when $n = 1 \rightarrow 100$ and expect that the implementation can be made even more efficient by parallel computing since the n sequence updates in Step 5 can be made independently in-between the $h_{i,j}$ and $g_{i,j}$ updates (see, e.g., refs. 87–89 for more sophisticated parallel WL algorithm implementations). The sought-after distribution, $P(\text{SCD}, \kappa) \approx g_{i,j}/\Delta\text{SCD}\Delta\kappa$ up to discretization errors, is now shown in the right panel of Fig. S1a as well as maintext Fig. 1a.

Given this $P(\text{SCD}, \kappa)$, the moderate degree to which SCD and κ are correlated may be quantified by the Pearson correlation coefficient

$$r = \frac{\langle (\text{SCD} - \langle \text{SCD} \rangle) (\kappa - \langle \kappa \rangle) \rangle}{\sqrt{\langle \text{SCD}^2 \rangle - \langle \text{SCD} \rangle^2} \sqrt{\langle \kappa^2 \rangle - \langle \kappa \rangle^2}} \approx -0.684, \quad (\text{S5})$$

where $\langle \dots \rangle$ here denotes average over the GA/WL-sampled $P(\text{SCD}, \kappa)$ distribution (thus the r value between $-\text{SCD}$ and κ is 0.684). The 26 overall-neutral polyampholyte sequences studied in this work are given in maintext Fig. 1b and in Table S1, their SCD and κ values are listed in Fig. S1 and plotted on the $-\text{SCD}$ versus κ plane in maintext Fig. 1a.

Field-theoretic formulation of polyampholyte conformations and phase separation

We study these model polyampholyte chain sequences using a field-theoretic formulation—using field-theoretic simulation (FTS) and random phase approximation (RPA)—as well as coarse-grained molecular dynamics (MD). As in our previous works (reviewed in ref. 68), the present field-theoretic formulation is based on a Hamiltonian \hat{H} that accounts for chain connectivity, short-spatial-range excluded-volume repulsion and long-spatial-range electrostatic interactions for a system of n_p polymers (polyampholyte chains) each consisting of N_p monomer (beads). \hat{H} is given by

$$\beta\hat{H} = \frac{3}{2b^2} \sum_{i=1}^{n_p} \sum_{\alpha=1}^{N_p-1} (\mathbf{R}_{i,\alpha+1} - \mathbf{R}_{i,\alpha})^2 + \frac{v}{2} \int d\mathbf{r} \hat{\rho}_{\text{tot}}(\mathbf{r})^2 + \frac{l_B}{2} \int d\mathbf{r} \int d\mathbf{r}' \frac{\hat{c}(\mathbf{r})\hat{c}(\mathbf{r}')}{|\mathbf{r} - \mathbf{r}'|}, \quad (\text{S6})$$

where $\beta \equiv 1/k_{\text{B}}T$ (k_{B} is the Boltzmann constant and T is absolute temperature), b is the reference root-mean-square bond length between two adjacent monomers along the chain sequence when non-bonded interactions are absent, $\mathbf{R}_{i,\alpha}$ is the position vector of the α th bead of the i th chain, $\hat{\rho}_{\text{tot}}(\mathbf{r})$ is bead number density (matter density), $\hat{c}(\mathbf{r})$ is charge density, v is the excluded volume parameter and $l_{\text{B}} = e^2/(4\pi\epsilon_0\epsilon_{\text{r}}k_{\text{B}}T)$ is the Bjerrum length that we use to quantify electrostatic interaction strength, with e denoting the protonic charge, ϵ_0 and ϵ_{r} are vacuum and relative permittivities, respectively; and temperature in our field-theoretical models is quantified by the reduced temperature $T^* \equiv b/l_{\text{B}}$. An electric charge σ_{α} is associated with the α th bead of each chain. In this work, we consider only overall charge neutral polyampholyte sequences, thus $\sum_{\alpha=1}^{N_{\text{p}}} \sigma_{\alpha} = 0$. To avoid potential singularities arising from modeling polymer beads as point particles, we model each bead as a normalized Gaussian distribution given by $\Gamma(\mathbf{r}) = \exp(-r^2/2\bar{a}^2)/(2\pi\bar{a}^2)^{3/2}$ where $r^2 \equiv |\mathbf{r}|^2$ (refs. 67, 90). Accordingly, the bead number density and charge density are given, respectively, by

$$\begin{aligned}\hat{\rho}_{\text{tot}}(\mathbf{r}) &= \sum_{i=1}^{n_{\text{p}}} \sum_{\alpha=1}^{N_{\text{p}}} \Gamma(\mathbf{r} - \mathbf{R}_{i,\alpha}), \\ \hat{c}(\mathbf{r}) &= \sum_{i=1}^{n_{\text{p}}} \sum_{\alpha=1}^{N_{\text{p}}} \sigma_{\alpha} \Gamma(\mathbf{r} - \mathbf{R}_{i,\alpha}).\end{aligned}\tag{S7}$$

The field-theoretic model system defined by Eqs. S6 and S7 is analyzed using random phase approximation (RPA) and field-theoretic simulation (FTS).

Random phase approximation (RPA). An approximate analytical theory, termed RPA, can be derived from the partition function formulated by path integrals based upon the Hamiltonian in Eq. S6. In the present study, all RPA calculations are performed within the context of an implicit solvent polymer field theory³⁰ (no explicit solvent, unlike, e.g., in ref. 29) with contact-excluded volume interactions and unscreened Coulomb electrostatic interactions as specified by Eq. S6 and, as mentioned, UV (short-distance)-divergences are regulated by Gaussian-smearred beads involving the function $\Gamma(\mathbf{r})$ as described above. In the present RPA calculations, we use a fixed excluded volume parameter $v = 0.0068b^3$ and a Gaussian smearing length of $\bar{a} = b/\sqrt{6}$. The detailed mathematical formulation and the computer code employed for our RPA calculations are documented and available through our recent review.⁶⁸ Examples of phase diagrams computed using FTS and RPA for the 26 polyampholyte sequences we study (maintext Fig. 1b, Fig. S1b, Table S1) are provided in maintext Fig. 1d. A complete list of these phase diagrams are documented in Fig. S2. The critical temperatures of these sequences' phase transitions in RPA and FTS are tabulated in Fig. S1b, whereas the necessary details of our FTS methodology are provided below.

Radius of gyration and contact maps of chain conformations in the field-theoretic formulation. As a novel extension of our previous field-theoretic formulation, we now connect the radius of gyration (R_{g}) of a single polymer chain to the polymer beads'

pair-correlation function³⁰ as follows:

$$\begin{aligned}
 R_g^2 &= \frac{1}{2N_p^2} \left\langle \sum_{\alpha=1}^{N_p} \sum_{\beta=1}^{N_p} (\mathbf{R}_\alpha - \mathbf{R}_\beta)^2 \right\rangle \\
 &= \frac{1}{2N_p^2} \int d\mathbf{r} \int d\mathbf{r}' \langle \hat{\rho}_c(\mathbf{r}) \hat{\rho}_c(\mathbf{r}') \rangle (\mathbf{r} - \mathbf{r}')^2,
 \end{aligned} \tag{S8}$$

where the bead center density is defined here by $\hat{\rho}_c(\mathbf{r}) = \sum_{\alpha=1}^{N_p} \delta(\mathbf{r} - \mathbf{R}_\alpha)$ and $\langle \dots \rangle$ denotes thermal averaging. Since the pair-correlation function $G(|\mathbf{r} - \mathbf{r}'|) = \langle \hat{\rho}_c(\mathbf{r}) \hat{\rho}_c(\mathbf{r}') \rangle$ depends only on the relative distance, we may perform a coordinate transformation such that $\mathbf{R} = (\mathbf{r} + \mathbf{r}')/2$ and $\mathbf{r} = \mathbf{r} - \mathbf{r}'$, with the associated Jacobian's determinant $|J| = 1$, and thus rewrite Eq. (S8) as

$$\begin{aligned}
 R_g^2 &= \frac{1}{2N_p^2} \int d\mathbf{R} \int d\mathbf{r} G(|\mathbf{r}|) |\mathbf{r}|^2 \\
 &= \frac{V}{2N_p^2} \int d\mathbf{r} G(|\mathbf{r}|) |\mathbf{r}|^2,
 \end{aligned} \tag{S9}$$

where $V = \int d\mathbf{R}$ is the volume of the system. Because we have elected to use smeared Gaussian packets instead of point particles in our field-theoretic formulation to regularize short-range divergences as noted above, we will approximate the δ -function defined pair-correlation function defined above by smeared densities instead. Accordingly, in the formulation below for calculating of R_g , we replace $G(|\mathbf{r} - \mathbf{r}'|)$ in Eq. (S8) by $\mathcal{C}(|\mathbf{r} - \mathbf{r}'|) = \langle \hat{\rho}(\mathbf{r}) \hat{\rho}(\mathbf{r}') \rangle$ where $\hat{\rho}(\mathbf{r}) = \sum_{\alpha=1}^{N_p} \Gamma(\mathbf{r} - \mathbf{R}_\alpha)$ as in Eq. (S7). Mathematically, $\mathcal{C}(r)$ (where $r = |\mathbf{r}|$) is expected to be different from $G(r)$ only in these functions' variations over short distances $\lesssim \bar{a}$. Since $G(r)$ is integrated and weighted by $|\mathbf{r}|^2 = r^2$ in Eq. S9 for R_g^2 , the replacement of $G(r)$ by $\mathcal{C}(r)$ is not numerically significant for the accuracy of the computed value of R_g . For our purpose, however, the smearing that replace $G(r)$ by $\mathcal{C}(r)$ is important as it allows $G(r)$ and thus R_g to be computed approximately using FTS.

By construction, Eq. S9 is applicable only for a single chain and needs to be extended for a multi-chain system. To do so, consider n_p identical chains in a polyampholyte solution. We now choose one chain at random and recognize it as “tagged”. We denote the rest of the $n_p - 1$ chains as “rest”. The total bead density can now be rewritten as $\hat{\rho}_{\text{tot}}(\mathbf{r}) = \hat{\rho}^{(t)}(\mathbf{r}) + \hat{\rho}^{(r)}(\mathbf{r})$ where the superscripts “(t)” and “(r)” refer to “tagged” and “rest”, respectively. With this setup, we can now substitute the smeared self-correlation function of the tagged chain $\mathcal{C}^{(t)}(r)$ for $G(r)$ in Eq. S9 to find the tagged chain's R_g^2 in the multi-chain system, and can simply set $n_p = 1$ in this general formulation to recover the formula for the R_g^2 of a single isolated chain. For clarity, we will denote this latter isolated-chain smeared self-correlation function by $\mathcal{C}^{(\text{isol})}(r)$.

Correlation functions can also be utilized to compute residue-residue (bead-bead, or monomer-monomer) contact maps. To do so we only have to identify the monomers' sequence positions along the polymer chains by rewriting the total bead center density for a multi-chain system as $\hat{\rho}_{c,\text{tot}}(\mathbf{r}) = \sum_{\alpha=1}^{N_p} \hat{\rho}_{c,\alpha}^{(t)}(\mathbf{r}) + \sum_{\alpha=1}^{N_p} \hat{\rho}_{c,\alpha}^{(r)}(\mathbf{r})$, where $\hat{\rho}_{c,\alpha}^{(t/r)}(\mathbf{r})$ is sequence-

position-specific density of the center of the α th bead in the “tagged” chain/“rest” chains. As specified above for Eq. S8, unlike the smeared $\hat{\rho}(\mathbf{r})$ defined above, the bead center density $\hat{\rho}_c(\mathbf{r})$ (with subscript “c”) is defined by δ -function of position without Γ smearing. We use unsmeared bead center densities for the computation of contacts because contacts are defined by spatial separations between bead centers. Now, the corresponding bead-specific unsmeared correlation functions can be defined as $G_{\alpha,\beta}^{(x),(y)}(|\mathbf{R}|) = \langle \hat{\rho}_{c,\alpha}^{(x)}(\mathbf{r}) \hat{\rho}_{c,\alpha}^{(y)}(\mathbf{r} + \mathbf{R}) \rangle$ where $\{x, y\} \in \{t, r\}$. With this definition, we can compute the average contact frequency between the (x, α) and (y, β) monomers (beads) by spatially integrating the corresponding $G_{\alpha,\beta}^{(x),(y)}(|\mathbf{R}|)$ from radial distance $|\mathbf{R}| = 0$ up to a suitably chosen cutoff in $|\mathbf{R}|$ for defining a contact, with the $x = y$ and $x \neq y$ cases accounting, respectively, for intrachain and interchain contacts. For the present work, we adopt the definitions

$$\omega_{\alpha,\beta}^{(t),(t)} = V \int_0^{2b} d\mathbf{r} G_{\alpha,\beta}^{(t),(t)}(|\mathbf{r}|), \quad (\text{S10a})$$

$$\omega_{\alpha,\beta}^{(t),(r)} = V \int_0^{2b} d\mathbf{r} G_{\alpha,\beta}^{(t),(r)}(|\mathbf{r}|), \quad (\text{S10b})$$

as intrachain (Eq. S10a) and interchain (Eq. S10b) contact frequencies, wherein a radial cutoff distance of $2b$ is used for defining a bead-bead spatial contact.

Key steps in the field-theoretic simulation (FTS). Using the expression for the Hamiltonian in Eq. S6, the canonical partition function of our system of interest is given by

$$\mathcal{Z} = \frac{1}{n_p!} \left(\prod_{i=1}^{n_p} \prod_{\alpha=1}^{N_p} \int d\mathbf{R}_{i,\alpha} \right) e^{-\beta \hat{H}}. \quad (\text{S11})$$

Following standard procedures,^{30,48,56,66,68} we derive a field theory described by a field Hamiltonian H (different from \hat{H}) such that the partition function itself remains same as Eq. S11 up to an inconsequential overall multiplicative constant, viz.,

$$\mathcal{Z} = \frac{V^{n_p}}{n_p!} \int \mathcal{D}w \int \mathcal{D}\psi e^{-H[w,\psi]}, \quad (\text{S12})$$

in which two fluctuating auxiliary fields w and ψ are introduced, with

$$H[w, \psi] = \int d\mathbf{r} \left[\frac{w(\mathbf{r})^2}{2v} + \frac{(\nabla\psi(\mathbf{r}))^2}{8\pi l_B} \right] - n_p \ln Q_p[\check{w}, \check{\psi}], \quad (\text{S13})$$

where $\check{\phi}(\mathbf{r}) = \Gamma \star \phi \equiv \int d\mathbf{r}' \Gamma(\mathbf{r} - \mathbf{r}') \phi(\mathbf{r}')$, $\phi = w, \psi$, with “ \star ” denoting this spatial convolution henceforth. In Eq. S13, the single-chain partition function Q_p is given by

$$Q_p[\check{w}, \check{\psi}] = \frac{1}{V} \int d\mathbf{R}_{N_p} \left(\prod_{\alpha=1}^{N_p-1} \int d\mathbf{R}_\alpha G^0(\mathbf{R}_{\alpha+1} - \mathbf{R}_\alpha | b) \right) e^{-i \sum_{\alpha=1}^{N_p} [\check{w}(\mathbf{R}_\alpha) + \sigma_\alpha \check{\psi}(\mathbf{R}_\alpha)]}, \quad (\text{S14})$$

where $i^2 = -1$ is the imaginary unit and

$$G^0(\mathbf{r}|b) = \left(\frac{3}{2\pi b^2}\right)^{3/2} e^{-3|\mathbf{r}|^2/2b^2}. \quad (\text{S15})$$

Based on this particle-to-field reformulation, the equilibrium properties of the system can now be studied through the dynamics of the fields. Since the field Hamiltonian H involves complex variables, we adopt⁵⁶ a ‘‘Complex Langevin’’ (CL) prescription^{59,60} inspired by stochastic quantization^{91,92} for computing averages for the system defined by Eq. S13 by introducing dependence on a fictitious time to the fields, which then evolve dynamically in accordance to the Langevin equations

$$\begin{aligned} \frac{\partial w(\mathbf{r}, t)}{\partial t} &= - \left[i\tilde{\rho}_{\text{tot}}(\mathbf{r}, t) + \frac{w(\mathbf{r}, t)}{v} \right] + \eta_w(\mathbf{r}, t), \\ \frac{\partial \psi(\mathbf{r}, t)}{\partial t} &= - \left[i\tilde{c}(\mathbf{r}, t) - \frac{\nabla^2 \psi(\mathbf{r}, t)}{4\pi l_B} \right] + \eta_\psi(\mathbf{r}, t), \end{aligned} \quad (\text{S16})$$

where t is a fictitious time, η_w and η_ψ are fields of real-valued random numbers drawn from a normal distribution of zero mean and standard deviation that is nonzero only when $t = t'$ and $\mathbf{r} = \mathbf{r}'$ [$\propto 2\delta(t - t')\delta(\mathbf{r} - \mathbf{r}')$], specifically, $\langle \eta_\phi(\mathbf{r}, t)\eta_{\phi'}(\mathbf{r}', t') \rangle = 2\delta_{\phi, \phi'}\delta(\mathbf{r} - \mathbf{r}')\delta(t - t')$. This is the basic Langevin formulation of FTS. In Eq. S16, $\tilde{\rho}_{\text{tot}}$ and \tilde{c} are field operators for total bead density and charge density, respectively, which may be expressed as

$$\begin{aligned} \tilde{\rho}_{\text{tot}}(\mathbf{r}) &= \Gamma \star \frac{n_p}{Q_p V} \sum_{\alpha=1}^{N_p} q_B(\mathbf{r}, \alpha) q_F(\mathbf{r}, \alpha) e^{i\check{w}(\mathbf{r}) + i\sigma_\alpha \check{\psi}(\mathbf{r})}, \\ \tilde{c}(\mathbf{r}) &= \Gamma \star \frac{n_p}{Q_p V} \sum_{\alpha=1}^{N_p} \sigma_\alpha q_B(\mathbf{r}, \alpha) q_F(\mathbf{r}, \alpha) e^{i\check{w}(\mathbf{r}) + i\sigma_\alpha \check{\psi}(\mathbf{r})}, \end{aligned} \quad (\text{S17})$$

where the forward (F) and backward (B) chain propagators q_F and q_B are constructed iteratively:

$$\begin{aligned} q_F(\mathbf{r}, \alpha + 1) &= e^{-i\check{w}(\mathbf{r}) - i\sigma_{\alpha+1} \check{\psi}(\mathbf{r})} \int d\mathbf{r}' G^0(\mathbf{r} - \mathbf{r}'|b) q_F(\mathbf{r}', \alpha), \\ q_B(\mathbf{r}, \alpha - 1) &= e^{-i\check{w}(\mathbf{r}) - i\sigma_{\alpha-1} \check{\psi}(\mathbf{r})} \int d\mathbf{r}' G^0(\mathbf{r} - \mathbf{r}'|b) q_B(\mathbf{r}', \alpha), \end{aligned} \quad (\text{S18})$$

with $q_F(\mathbf{r}, 1) = e^{-i\check{w}(\mathbf{r}) - i\sigma_1 \check{\psi}(\mathbf{r})}$ and $q_B(\mathbf{r}, N_p) = e^{-i\check{w}(\mathbf{r}) - i\sigma_{N_p} \check{\psi}(\mathbf{r})}$.

In practice, the differential field evolution equations Eqs. S16 have to be numerically solved in discretized space and discretized CL time. For the present work, every FTS is conducted in a $32 \times 32 \times 32$ cubic grid with a side length $32\bar{a}$ and we set $\bar{a} = b/\sqrt{6}$ following previous works. A CL time step $dt = 0.005$ and a semi-implicit CL time integration scheme⁹³ are employed. To compute the thermal average of any thermodynamic observable by FTS, the particle-based thermal average has to be replaced by an average over the field configurations of the corresponding field operator. The field operators could be derived

by introducing appropriate “source” terms (fields) in the particle picture Hamiltonian (“ J ” fields, see below), as is commonly practiced in theoretical particle physics.⁹⁴ If an observable $\hat{\mathcal{O}}(\mathbf{r})$ has a field operator $\tilde{\mathcal{O}}(w, \psi)$, then in practice the equilibrium field average of that specific operator is evaluated as an asymptotic CL time average through

$$\left\langle \hat{\mathcal{O}}(\{\mathbf{R}_{i,\alpha}\}) \right\rangle = \left\langle \tilde{\mathcal{O}}[w, \psi] \right\rangle_{\text{F}} = \frac{\int \mathcal{D}w \int \mathcal{D}\psi \tilde{\mathcal{O}}(w, \psi) e^{-H[w, \psi]}}{\int \mathcal{D}w \int \mathcal{D}\psi e^{-H[w, \psi]}} = \frac{1}{M} \sum_{j=1}^M \tilde{\mathcal{O}}[w(\mathbf{r}, t_j), \psi(\mathbf{r}, t_j)] , \quad (\text{S19})$$

where M is the maximum number of field configurations considered (configurations are labeled by j in the above equation for selected values t_j of fictitious time t) and $\langle \cdot \cdot \cdot \rangle_{\text{F}}$ denotes field averaging. The configurations at t_j s and the total number of configurations M used in the averaging are chosen such that the real part of the field averaged quantity has a reasonably small fluctuation over independent simulation runs and the corresponding imaginary part is approximately zero. For all the FTS computation, we set the excluded volume parameter $v = 0.0068b^3$. Further details of our approach can be found in ref. 68.

FTS operators for correlation functions in the computation of polymer radius of gyration. As outlined above in the discussion preceding Eq. S10, to compute equilibrium properties of individual polymer chains in a multiple-chain system, we consider one chain, chosen at random, as tagged. The total bead density in Eq. S7 can then be rewritten as

$$\hat{\rho}_{\text{tot}}(\mathbf{r}) = \hat{\rho}^{(\text{t})}(\mathbf{r}) + \hat{\rho}^{(\text{r})}(\mathbf{r}) , \quad (\text{S20})$$

where the superscripts “(t)” and “(r)” denote ‘tagged’ and ‘rest’, respectively, with $\hat{\rho}^{(\text{t})}(\mathbf{r})$ for the tagged chain and $\hat{\rho}^{(\text{r})}(\mathbf{r})$ for the rest of the chains (untagged chains) given by

$$\begin{aligned} \hat{\rho}^{(\text{t})}(\mathbf{r}) &= \sum_{\alpha=1}^{N_p} \Gamma(\mathbf{r} - \mathbf{R}_{\alpha}^{(\text{t})}) , \\ \hat{\rho}^{(\text{r})}(\mathbf{r}) &= \sum_{i=1}^{n_p-1} \sum_{\alpha=1}^{N_p} \Gamma(\mathbf{r} - \mathbf{R}_{i,\alpha}^{(\text{r})}) . \end{aligned} \quad (\text{S21})$$

Field operators for total bead densities of “tagged” and “rest” chains are identified by introducing the source terms $J^{(\text{t})}$ and $J^{(\text{r})}$ in the original particle-picture Hamiltonian in Eq. S6 in the following manner:

$$\beta \hat{H} \rightarrow \beta \hat{H}[J^{(\text{t})}, J^{(\text{r})}] = \beta \hat{H} - \int d\mathbf{r} J^{(\text{t})}(\mathbf{r}) \hat{\rho}^{(\text{t})}(\mathbf{r}) - \int d\mathbf{r} J^{(\text{r})}(\mathbf{r}) \hat{\rho}^{(\text{r})}(\mathbf{r}) . \quad (\text{S22})$$

The resulting source-dependent partition function is now given by

$$\mathcal{Z}[J^{(\text{t})}, J^{(\text{r})}] \sim \left(\prod_{\alpha=1}^{N_p} \int d\mathbf{R}_{\alpha}^{(\text{t})} \right) \left(\prod_{i=1}^{n_p-1} \prod_{\alpha=1}^{N_p} \int d\mathbf{R}_{i,\alpha}^{(\text{r})} \right) e^{-\beta \hat{H}[J^{(\text{t})}, J^{(\text{r})}]} . \quad (\text{S23})$$

From this last expression (Eq. S23), we obtain the formal relations

$$\begin{aligned}\langle \hat{\rho}^{(t)}(\mathbf{r}) \rangle &= \left(\frac{1}{\mathcal{Z}[J^{(t)}, J^{(r)}]} \frac{\delta \mathcal{Z}[J^{(t)}, J^{(r)}]}{\delta J^{(t)}(\mathbf{r})} \right)_{J^{(t)}=J^{(r)}=0}, \\ \langle \hat{\rho}^{(r)}(\mathbf{r}) \rangle &= \left(\frac{1}{\mathcal{Z}[J^{(t)}, J^{(r)}]} \frac{\delta \mathcal{Z}[J^{(t)}, J^{(r)}]}{\delta J^{(r)}(\mathbf{r})} \right)_{J^{(t)}=J^{(r)}=0},\end{aligned}\quad (\text{S24})$$

where $\langle \dots \rangle$ denotes thermal averaging. In the corresponding field theory representation, we have

$$\mathcal{Z}[J^{(t)}, J^{(r)}] \sim \int \mathcal{D}w \int \mathcal{D}\psi e^{-H[w, \psi, J^{(t)}, J^{(r)}]}, \quad (\text{S25})$$

where

$$\begin{aligned}H[w, \psi, J^{(t)}, J^{(r)}] &= \int d\mathbf{r} \left[\frac{w(\mathbf{r})^2}{2v} + \frac{(\nabla \psi(\mathbf{r}))^2}{8\pi l_B} \right] \\ &\quad - \ln Q_p[\check{w} - i\check{J}^{(t)}, \check{\psi}] - (n_p - 1) \ln Q_p[\check{w} - i\check{J}^{(r)}, \check{\psi}].\end{aligned}\quad (\text{S26})$$

In this equation (Eq. S26), Q_p has the same functional form as that in Eq. S14. We can now apply the definitions Eq. S24 to Eq. S25 to arrive at $\langle \hat{\rho}^{(t)}(\mathbf{r}) \rangle = \langle \tilde{\rho}^{(t)}(\mathbf{r}) \rangle_F$ and $\langle \hat{\rho}^{(r)}(\mathbf{r}) \rangle = \langle \tilde{\rho}^{(r)}(\mathbf{r}) \rangle_F$ where

$$\begin{aligned}\tilde{\rho}^{(t)}(\mathbf{r}) &= \frac{1}{n_p} \tilde{\rho}_{\text{tot}}(\mathbf{r}), \\ \tilde{\rho}^{(r)}(\mathbf{r}) &= \frac{n_p - 1}{n_p} \tilde{\rho}_{\text{tot}}(\mathbf{r}),\end{aligned}\quad (\text{S27})$$

and $\tilde{\rho}_{\text{tot}}(\mathbf{r})$ is defined in Eq. S17 and, again, $\langle \dots \rangle_F$ represents average over field configurations.

We can also compute the self-correlation function of the tagged chain from the partition function in Eq. S23 through the formal relation

$$\mathcal{C}^{(t)}(|\mathbf{r} - \mathbf{r}'|) = \langle \hat{\rho}^{(t)}(\mathbf{r}) \hat{\rho}^{(t)}(\mathbf{r}') \rangle = \left(\frac{1}{\mathcal{Z}[J^{(t)}, J^{(r)}]} \frac{\delta^2 \mathcal{Z}[J^{(t)}, J^{(r)}]}{\delta J^{(t)}(\mathbf{r}) \delta J^{(t)}(\mathbf{r}')} \right)_{J^{(t)}=J^{(r)}=0}. \quad (\text{S28})$$

Applying this relation (Eq. S28) to Eq. S23 results in

$$\mathcal{C}^{(t)}(|\mathbf{r} - \mathbf{r}'|) = \frac{i}{v} \langle w(\mathbf{r}) \tilde{\rho}_{\text{tot}}(\mathbf{r}') \rangle_F - \langle \tilde{\rho}^{(t)}(\mathbf{r}) \tilde{\rho}^{(r)}(\mathbf{r}') \rangle_F, \quad (\text{S29})$$

where, following ref. 30, we have avoided computing a functional double derivative of Q_p .

When there is only a single isolated chain in the system, the self-correlation function is obtained by setting $n_p = 1$ and $\tilde{\rho}^{(r)}(\mathbf{r}') = 0$ in the above derivation, yielding

$$\mathcal{C}^{(\text{isol})}(|\mathbf{r} - \mathbf{r}'|) = \frac{i}{v} \langle w(\mathbf{r}) \tilde{\rho}_{\text{tot}}(\mathbf{r}') \rangle_F. \quad (\text{S30})$$

Utilizing translational invariance of our systems, we can write

$$\begin{aligned}\langle \hat{\rho}(\mathbf{r})\hat{\rho}(\mathbf{r}') \rangle &= \frac{1}{V} \int d\mathbf{r}'' \langle \hat{\rho}(\mathbf{r} + \mathbf{r}'')\hat{\rho}(\mathbf{r}' + \mathbf{r}'') \rangle \\ &= \frac{1}{V} \int \frac{d\mathbf{k}}{(2\pi)^3} e^{-i\mathbf{k}\cdot(\mathbf{r}-\mathbf{r}')} \langle \check{\rho}(\mathbf{k})\check{\rho}(-\mathbf{k}) \rangle,\end{aligned}\tag{S31}$$

where, when the density smearing described above is applied, $\check{\rho}(\mathbf{k}) \equiv \int d\mathbf{r} e^{i\mathbf{k}\cdot\mathbf{r}} \hat{\rho}(\mathbf{r})$ is the Fourier transform of the smeared density $\hat{\rho}(\mathbf{r})$. In that case, it follows that $\check{\rho}(\mathbf{k}) = \check{\Gamma}(\mathbf{k})\check{\rho}_c(\mathbf{k})$ where $\check{\Gamma}(\mathbf{k}) = e^{-\bar{a}^2|\mathbf{k}|^2/2}$ is the Fourier transform of the smearing function $\Gamma(\mathbf{r})$ and $\check{\rho}_c(\mathbf{k})$ is the Fourier transform of the bead center density $\hat{\rho}_c(\mathbf{r})$. This implies that when Gaussian smearing is utilized in our formulation, the bead center-bead center pair correlation function [$G(r) \rightarrow \mathcal{C}(r)$] can now be expressed as

$$\langle \hat{\rho}_c(\mathbf{r})\hat{\rho}_c(\mathbf{r}') \rangle = \frac{1}{V} \int \frac{d\mathbf{k}}{(2\pi)^3} e^{-i\mathbf{k}\cdot(\mathbf{r}-\mathbf{r}')} \frac{\langle \check{\rho}(\mathbf{k})\check{\rho}(-\mathbf{k}) \rangle}{\check{\Gamma}(\mathbf{k})^2}.\tag{S32}$$

FTS operators for correlation functions in the computation of contact maps of polymers. As noted above, the starting point for contact map computations is the (unsmeared) bead center density correlation functions. As noted above in the discussion preceding Eq. S10, we first rewrite the total bead center density as

$$\hat{\rho}_{c,\text{tot}}(\mathbf{r}) = \hat{\rho}_c^{(t)}(\mathbf{r}) + \hat{\rho}_c^{(r)}(\mathbf{r}),\tag{S33}$$

where $\hat{\rho}_c^{(t)}(\mathbf{r})$ and $\hat{\rho}_c^{(r)}(\mathbf{r})$ could be expressed in terms of the bead-position-specific densities along the chains through

$$\begin{aligned}\hat{\rho}_c^{(t)}(\mathbf{r}) &= \sum_{\alpha=1}^{N_p} \hat{\rho}_{c,\alpha}^{(t)}(\mathbf{r}) = \sum_{\alpha=1}^{N_p} \delta(\mathbf{r} - \mathbf{R}_\alpha^{(t)}) , \\ \hat{\rho}_c^{(r)}(\mathbf{r}) &= \sum_{\alpha=1}^{N_p} \hat{\rho}_{c,\alpha}^{(r)}(\mathbf{r}) = \sum_{i=1}^{n_p-1} \sum_{\alpha=1}^{N_p} \delta(\mathbf{r} - \mathbf{R}_{i,\alpha}^{(r)}) .\end{aligned}\tag{S34}$$

We now introduce monomer (residue)-specific source terms in the interaction Hamiltonian Eq. S6:

$$\beta\hat{H} \rightarrow \beta\hat{H}[\{J_\alpha^{(t)}\}, \{J_\alpha^{(r)}\}] = \beta\hat{H} - \int d\mathbf{r} \sum_{\alpha=1}^N J_\alpha^{(t)}(\mathbf{r})\hat{\rho}_{c,\alpha}^{(t)}(\mathbf{r}) - \int d\mathbf{r} \sum_{\alpha=1}^N J_\alpha^{(r)}(\mathbf{r})\hat{\rho}_{c,\alpha}^{(r)}(\mathbf{r}).\tag{S35}$$

The corresponding partition function is

$$\mathcal{Z}[\{J_\alpha^{(t)}\}, \{J_\alpha^{(r)}\}] \sim \left(\prod_{\alpha=1}^{N_p} \int d\mathbf{R}_\alpha^{(t)} \right) \left(\prod_{i=1}^{n_p-1} \prod_{\alpha=1}^{N_p} \int d\mathbf{R}_{i,\alpha}^{(r)} \right) e^{-\beta \hat{H}[\{J_\alpha^{(t)}\}, \{J_\alpha^{(r)}\}]} . \quad (\text{S36})$$

From this expression (Eq. S36), the average density of the α th bead center is formally

$$\langle \hat{\rho}_{c,\alpha}^{(x)}(\mathbf{r}) \rangle = \left(\frac{1}{\mathcal{Z}[\{J_\alpha^{(t)}\}, \{J_\alpha^{(r)}\}]} \frac{\delta \mathcal{Z}[\{J_\alpha^{(t)}\}, \{J_\alpha^{(r)}\}]}{\delta J_\alpha^{(x)}(\mathbf{r})} \right)_{\{J_\alpha^{(t)}\}=\{J_\alpha^{(r)}\}=0} , \quad (\text{S37})$$

and the correlation function between any two bead center is given by

$$G_{\alpha,\beta}^{(x),(y)}(|\mathbf{r} - \mathbf{r}'|) = \langle \hat{\rho}_{c,\alpha}^{(x)}(\mathbf{r}) \hat{\rho}_{c,\beta}^{(y)}(\mathbf{r}') \rangle = \left(\frac{1}{\mathcal{Z}[\{J_\alpha^{(t)}\}, \{J_\alpha^{(r)}\}]} \frac{\delta \mathcal{Z}[\{J_\alpha^{(t)}\}, \{J_\alpha^{(r)}\}]}{\delta J_\alpha^{(x)}(\mathbf{r}) \delta J_\beta^{(y)}(\mathbf{r}')} \right)_{\{J_\alpha^{(t)}\}=\{J_\alpha^{(r)}\}=0} \quad (\text{S38})$$

where $\{x, y\} \in \{t, r\}$. The corresponding partition function in the field picture is then given by

$$\mathcal{Z}[\{J_\alpha^{(t)}\}, \{J_\alpha^{(r)}\}] \sim \int \mathcal{D}w \int \mathcal{D}\psi e^{-H[w, \psi, \{J_\alpha^{(t)}\}, \{J_\alpha^{(r)}\}]} \quad (\text{S39})$$

where

$$H[w, \psi, \{J_\alpha^{(t)}\}, \{J_\alpha^{(r)}\}] = \int d\mathbf{r} \left[\frac{w(\mathbf{r})^2}{2v} + \frac{(\nabla \psi(\mathbf{r}))^2}{8\pi l_B} \right] - \ln Q_p[\check{w} - i\{J_\alpha^{(t)}\}, \check{\psi}] - (n_p - 1) \ln Q_p[\check{w} - i\{J_\alpha^{(r)}\}, \check{\psi}] , \quad (\text{S40})$$

and the absence of breve in the source terms on the right hand side in the above equation means that the source terms are not smeared. In Eq. S40, Q_p has the same functional form as that in Eq. S14, which can be written explicitly as

$$Q_p[\check{w} - i\{J_\alpha\}, \check{\psi}] = \frac{1}{V} \int d\mathbf{R}_{N_p} e^{-i\Psi_{N_p}} \int d\mathbf{R}_{N_p-1} G_{N_p, N_p-1}^0 e^{-i\Psi_{N_p-1}} \dots \dots \int d\mathbf{R}_\alpha G_{\alpha+1, \alpha}^0 e^{-i\Psi_\alpha} \dots \int d\mathbf{R}_1 G_{2,1}^0 e^{-i\Psi_1} , \quad (\text{S41})$$

where $\Psi_\alpha = \check{w}(\mathbf{R}_\alpha) + \sigma_\alpha \check{\psi}(\mathbf{R}_\alpha) + iJ_\alpha(\mathbf{R}_\alpha)$, and

$$G_{\alpha+1, \alpha}^0 \equiv G^0(\mathbf{R}_{\alpha+1} - \mathbf{R}_\alpha | b) \quad (\text{S42})$$

with G^0 defined by Eq. S15. Substituting Eq. S37 into Eq. S39 then results in $\langle \hat{\rho}_{c,\alpha}^{(t)}(\mathbf{r}) \rangle =$

$\langle \tilde{\rho}_{c,\alpha}^{(t)}(\mathbf{r}) \rangle_{\text{F}}$ and $\langle \hat{\rho}_{c,\alpha}^{(r)}(\mathbf{r}) \rangle = \langle \tilde{\rho}_{c,\alpha}^{(r)}(\mathbf{r}) \rangle_{\text{F}}$, with

$$\begin{aligned}\tilde{\rho}_{c,\alpha}^{(t)}(\mathbf{r}) &= \frac{1}{Q_{\text{p}}[\check{w}, \check{\psi}]V} q_B(\mathbf{r}, \alpha) q_F(\mathbf{r}, \alpha) e^{i\check{w}(\mathbf{r}) + i\sigma_{\alpha}\check{\psi}(\mathbf{r})}, \\ \tilde{\rho}_{c,\alpha}^{(r)}(\mathbf{r}) &= \frac{n_{\text{p}} - 1}{Q_{\text{p}}[\check{w}, \check{\psi}]V} q_B(\mathbf{r}, \alpha) q_F(\mathbf{r}, \alpha) e^{i\check{w}(\mathbf{r}) + i\sigma_{\alpha}\check{\psi}(\mathbf{r})}.\end{aligned}\tag{S43}$$

As discussed above in conjunction with eq. S10b, the numbers of interchain contacts and thus interchain contact maps are determined in our formulation via the cross correlation function between the α th bead center of the tagged chain and the β th bead center of the rest of the chains. This cross correlation is readily obtained by taking double functional derivatives of the partition function in Eq. S39 in accordance with Eq. S38 to yield

$$G_{\alpha,\beta}^{(t),(r)}(|\mathbf{r} - \mathbf{r}'|) = \langle \tilde{\rho}_{c,\alpha}^{(t)}(\mathbf{r}) \tilde{\rho}_{c,\beta}^{(r)}(\mathbf{r}') \rangle_{\text{F}}\tag{S44}$$

for the calculation of interchain numbers of contacts in Eq. S10b. Similarly, for the numbers of intrachain contacts and intrachain contact maps, we compute, in accordance with Eq. S10a, the correlations between the beads of the tagged chain as follows:

$$\begin{aligned}G_{\alpha,\beta}^{(t),(t)}(|\mathbf{r}|) &= \frac{1}{V} \int d\mathbf{R} \langle \hat{\rho}_{c,\alpha}^{(t)}(\mathbf{R}) \hat{\rho}_{c,\beta}^{(t)}(\mathbf{r} + \mathbf{R}) \rangle \\ &= \frac{1}{V} \int d\mathbf{R} \left(\frac{1}{\mathcal{Z}[\{J_{\alpha}^{(t)}\}, \{J_{\alpha}^{(r)}\}]} \frac{\delta \mathcal{Z}[\{J_{\alpha}^{(t)}\}, \{J_{\alpha}^{(r)}\}]}{\delta J_{\alpha}^{(t)}(\mathbf{R}) \delta J_{\beta}^{(t)}(\mathbf{r} + \mathbf{R})} \right)_{\{J_{\alpha}^{(t)}\} = \{J_{\alpha}^{(r)}\} = 0} \\ &= \frac{1}{V} \int d\mathbf{R} \left(\frac{1}{Q_{\text{p}}[\check{w} - i\{J_{\alpha}^{(t)}\}, \check{\psi}]} \frac{\delta^2 Q_{\text{p}}[\check{w} - i\{J_{\alpha}^{(t)}\}, \check{\psi}]}{\delta J_{\alpha}^{(t)}(\mathbf{R}) \delta J_{\beta}^{(t)}(\mathbf{R} + \mathbf{r})} \right)_{\{J_{\alpha}^{(t)}\} = 0} \\ &= \langle \tilde{G}_{\alpha,\beta}^{(t),(t)}(\mathbf{r}) \rangle_{\text{F}},\end{aligned}\tag{S45}$$

where

$$\begin{aligned}\tilde{G}_{\alpha,\beta}^{(t),(t)}(\mathbf{r}) &= \frac{1}{V} \int d\mathbf{R} \left[\frac{1}{V Q_{\text{p}}[\check{w}, \check{\psi}]} \int d\mathbf{R}_{N_{\text{p}}}^{(t)} e^{-i\Psi_{N_{\text{p}}}(\mathbf{R}_{N_{\text{p}}}^{(t)})} \int d\mathbf{R}_{N_{\text{p}}-1}^{(t)} G_{N_{\text{p}}, N_{\text{p}}-1}^0 e^{-i\Psi_{N_{\text{p}}-1}(\mathbf{R}_{N_{\text{p}}-1}^{(t)})} \dots \right. \\ &\quad \left. \dots \int d\mathbf{R}_2^{(t)} G_{3,2}^0 e^{-i\Psi_2(\mathbf{R}_2^{(t)})} \int d\mathbf{R}_1^{(t)} G_{2,1}^0 e^{-i\Psi_1(\mathbf{R}_1^{(t)})} \right] \delta(\mathbf{R} - \mathbf{R}_{\alpha}^{(t)}) \delta(\mathbf{R} + \mathbf{r} - \mathbf{R}_{\beta}^{(t)}) \\ &= \frac{1}{V Q_{\text{p}}[\check{w}, \check{\psi}]} \int \frac{d\mathbf{k}}{(2\pi)^3} \left[\frac{1}{V} \int d\mathbf{R}_{N_{\text{p}}}^{(t)} e^{-i\Psi_{N_{\text{p}}}(\mathbf{R}_{N_{\text{p}}}^{(t)})} \int d\mathbf{R}_{N_{\text{p}}-1}^{(t)} G_{N_{\text{p}}, N_{\text{p}}-1}^0 e^{-i\Psi_{N_{\text{p}}-1}(\mathbf{R}_{N_{\text{p}}-1}^{(t)})} \dots \right. \\ &\quad \left. \dots \int d\mathbf{R}_2^{(t)} G_{3,2}^0 e^{-i\Psi_2(\mathbf{R}_2^{(t)})} \int d\mathbf{R}_1^{(t)} G_{2,1}^0 e^{-i\Psi_1(\mathbf{R}_1^{(t)})} \right] e^{i\mathbf{k} \cdot (\mathbf{R}_{\beta}^{(t)} - \mathbf{R}_{\alpha}^{(t)} - \mathbf{r})} \\ &= \frac{1}{V Q_{\text{p}}} \int \frac{d\mathbf{k}}{(2\pi)^3} e^{-i\mathbf{k} \cdot \mathbf{r}} Q_{\text{p}}^{(\alpha,\beta)}(\mathbf{k}),\end{aligned}\tag{S46}$$

with $\Psi_\alpha = \check{w}(\mathbf{R}_\alpha^{(t)}) + \sigma_\alpha \check{\psi}(\mathbf{R}_\alpha^{(t)})$. In the last Eq. S46, $Q_p^{(\alpha,\beta)}(\mathbf{k})$ is a \mathbf{k} -dependent (Fourier-transformed) single chain restricted partition function, given by

$$Q_p^{(\alpha,\beta)}(\mathbf{k}) = \left[\frac{1}{V} \int d\mathbf{R}_{N_p}^{(t)} e^{-i\Psi_{N_p}(\mathbf{R}_{N_p}^{(t)})} \int d\mathbf{R}_{N_p-1}^{(t)} G_{N_p, N_p-1}^0 e^{-i\Psi_{N_p-1}(\mathbf{R}_{N_p-1}^{(t)})} \right. \\ \left. \dots \int d\mathbf{R}_2^{(t)} G_{3,2}^0 e^{-i\Psi_2(\mathbf{R}_2^{(t)})} \int d\mathbf{R}_1^{(t)} G_{2,1}^0 e^{-i\Psi_1(\mathbf{R}_1^{(t)})} \right] e^{i\mathbf{k} \cdot (\mathbf{R}_\beta^{(t)} - \mathbf{R}_\alpha^{(t)})}. \quad (\text{S47})$$

This implies that in order to evaluate $\tilde{G}_{\alpha,\beta}^{(t),(t)}(\mathbf{r})$ in Eq. S46, we need to first evaluate $Q_p^{(\alpha,\beta)}(\mathbf{k})$ at each \mathbf{k} and then perform an inverse Fourier transform according to the last equality in Eq. S46. Therefore, for a $N_L \times N_L \times N_L$ spatial (x, y, z) lattice used for FTS, ideally we should calculate the values of $Q_p^{(\alpha,\beta)}(\mathbf{k})$ on a (reciprocal) \mathbf{k} -space lattice of the same size, i.e., determine $Q_p^{(\alpha,\beta)}(\mathbf{k})$ $(N_L)^3$ times for each (α, β) pair for each field configuration (Eq. S47). This would be exceedingly computationally intensive. For computational efficiency, we consider instead a slightly more coarse-grained \mathbf{k} -space lattice of dimensions $N_{\mathbf{k}} \times N_{\mathbf{k}} \times N_{\mathbf{k}}$ with $N_{\mathbf{k}} = N_L/2$, such that the resolution of its reciprocal space, i.e., the original (x, y, z) space, becomes $(\Delta k_x, \Delta k_y, \Delta k_z) \equiv (4\pi/L, 4\pi/L, 4\pi/L)$ with $L = N_L \bar{a}$. Nonetheless, we still compute the $(\prod_\alpha \int d\mathbf{R}_\alpha)$ volume integrals in Eq. (S47) in the original $N_L \times N_L \times N_L$ spatial lattice with resolution $(\Delta x, \Delta y, \Delta z) = (\bar{a}, \bar{a}, \bar{a})$. In this way, we reduce the computational cost by ~ 8 times. Thus, for all the intrachain FTS contact maps presented here, $N_L = 32$, $N_{\mathbf{k}} = 16$, and the final equilibrium field configurations of 32 independent runs are used for field averaging. As a check on the accuracy of this coarse-graining, we have also computed contact maps with $N_{\mathbf{k}} = 8$ reciprocal lattice and saw no visible difference from the $N_{\mathbf{k}} = 16$ results.

Volume integration in simulation boxes with periodic boundary conditions.

To perform volume integration of an isotropic function $f(r)$ in a $L \times L \times L$ cubic box ($r \equiv |\mathbf{r}|$) with periodic boundary conditions, the integration measure dV has to be modified owing to the periodic boundary conditions, as follows:

$$dV(r) = \begin{cases} 4\pi r^2 dr, & 0 \leq r \leq L/2, \\ 2\pi r(3L - 4r) dr, & L/2 < r \leq \sqrt{2}L/2, \\ 2rL[3\pi - 12g_1(r/L) + g_2(r/L)] dr, & \sqrt{2}L/2 < r \leq \sqrt{3}L/2, \\ 0, & r > \sqrt{3}L/2, \end{cases} \quad (\text{S48})$$

where

$$g_1(x) = \tan^{-1} \sqrt{4x^2 - 2}, \\ g_2(x) = 8x \left\{ \tan^{-1} \left[\frac{2x(4x^2 - 3)}{\sqrt{4x^2 - 2}(4x^2 + 1)} \right] \right\}, \quad (\text{S49})$$

such that integration of any isotropic function $f(r)$ from $r = 0$ to any upper integration

limit $r = r_{\max}$ on the periodic lattice is specified by

$$\int_{|\mathbf{r}| \leq r_{\max}} d\mathbf{r} f(r) = \int_0^{r_{\max}} dV(r) f(r) \quad (\text{S50})$$

with $dV(r)$ defined in Eqs. S48 and S49 above.

Numerical estimation of T_{cr}^* in FTS Binodal phase boundaries in FTS are computed using the method described in ref. 68. In the present study, to estimate the critical temperature T_{cr}^* from the FTS binodals, we adopt—as in recent coarse-grained MD studies of biomolecular condensates^{37,62}—the scaling approach outlined in ref. 61, which assumes that low- and high-density phase concentrations, denoted by ρ_{L} and ρ_{H} , respectively, follow the relations

$$\frac{\rho_{\text{H}} + \rho_{\text{L}}}{2} = \rho_{\text{cr}} + A(T_{\text{cr}}^* - T^*) , \quad (\text{S51a})$$

$$\rho_{\text{H}} - \rho_{\text{L}} = \Delta\rho_0 \left(1 - \frac{T^*}{T_{\text{cr}}^*}\right)^\nu , \quad (\text{S51b})$$

where $\nu = 0.325$, and A , $\Delta\rho_0$, critical density ρ_{cr} , and T_{cr}^* are free fitting parameters. Now, for each sequence, we use the highest two simulated T^* for fitting. First, we estimate $\Delta\rho_0$ and T_{cr}^* by fitting the numerical values of $(\rho_{\text{H}} - \rho_{\text{L}})$ to Eq. S51b. Next, we apply this fitted T_{cr}^* to Eq. (S51a) to fit the numerical values of $(\rho_{\text{H}} + \rho_{\text{L}})/2$ to yield fitted values for ρ_{cr} and A . These fitted parameters are then applied to obtain ρ_{H} and ρ_{L} as functions of T^* from the two relations in Eq. S51. In Fig. S2 (see below) and maintext Fig. 1d, these fitted functions are used to construct continuous curves through the fitted $(\rho_{\text{cr}}, T_{\text{cr}}^*)$ critical point and the four simulated binodal (ρ_{L}, T^*) and (ρ_{H}, T^*) datapoints with the two highest T^* , whereas the numerical FTS (ρ_{L}, T^*) and (ρ_{H}, T^*) datapoints for the dilute and dense branches of the binodals for the rest of the simulated T^* are simply connected by lines as guides for the eye.

Coarse-grained molecular dynamics (MD) model of polyampholyte conformations and phase separation

The coarse-grained MD model here is essentially identical to the “hard-core repulsion” model we used previously in ref. 37 for the simulation of “sv”¹³ and “as”³⁷ polyampholyte sequences. The only difference is that the repulsive part of the Lennard-Jones (LJ) potential is set to zero for $r > 2^{1/6}a$ in the present study—where a is the reference (equilibrium) bond length between successive beads (monomers) along the chain sequence—instead of for $r > a$ in ref. 37. MD simulation in the present work is carried out using the protocol described in refs. 37, 48. A contact is defined to exist between two monomers when their center-of-mass spatial separation is within $2a$.

Supporting Figures

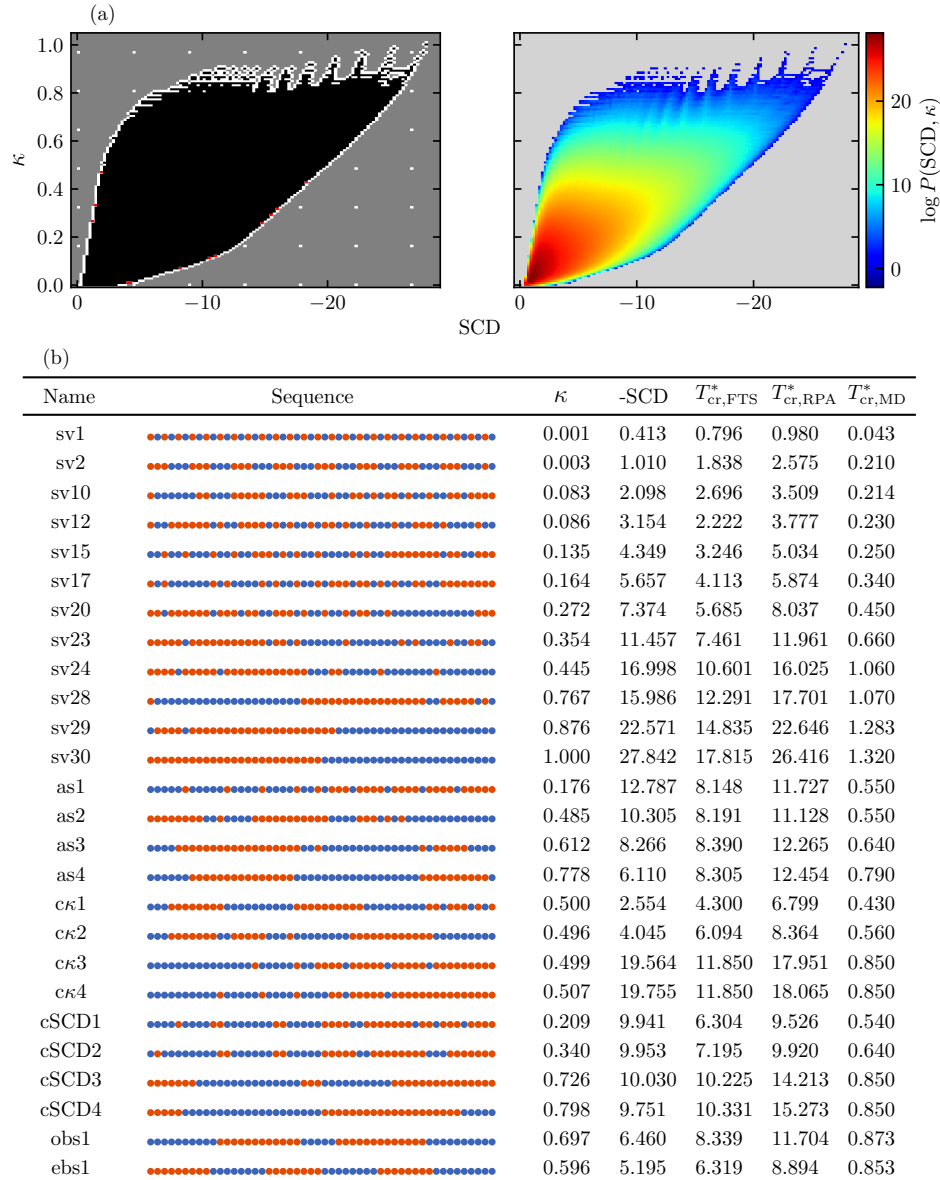


Fig. S1: Genetic-algorithm (GA) and Wang-Landau (WL) sampling of the SCD– κ sequence space of net-neutral 50mer polyampholytes. (a) *Left*– Results of the diversity-enhanced GA scan. Black region represents the region found by the GA to be populated by sequences. Bins containing target (SCD, κ) values for which no sequence was found by the GA are shown in white. Red bins indicate bins mislabelled by the GA as empty, i.e., bins for which the GA was not able to find a sequence but that the subsequent WL calculation revealed to be non-empty. Other regions where no sequence was found by either GA or WL are in gray. *Right*– Joint distribution $P(\text{SCD}, \kappa)$ computed using the WL algorithm. (b) The 26 net-neutral polyampholyte sequences studied in this work (same as those depicted in maintext Fig. 1b), their κ , SCD values as well their critical temperatures in the FTS, RPA, and MD models. Positively and negatively charged monomers along the sequences are represented, respectively, by blue and red beads.

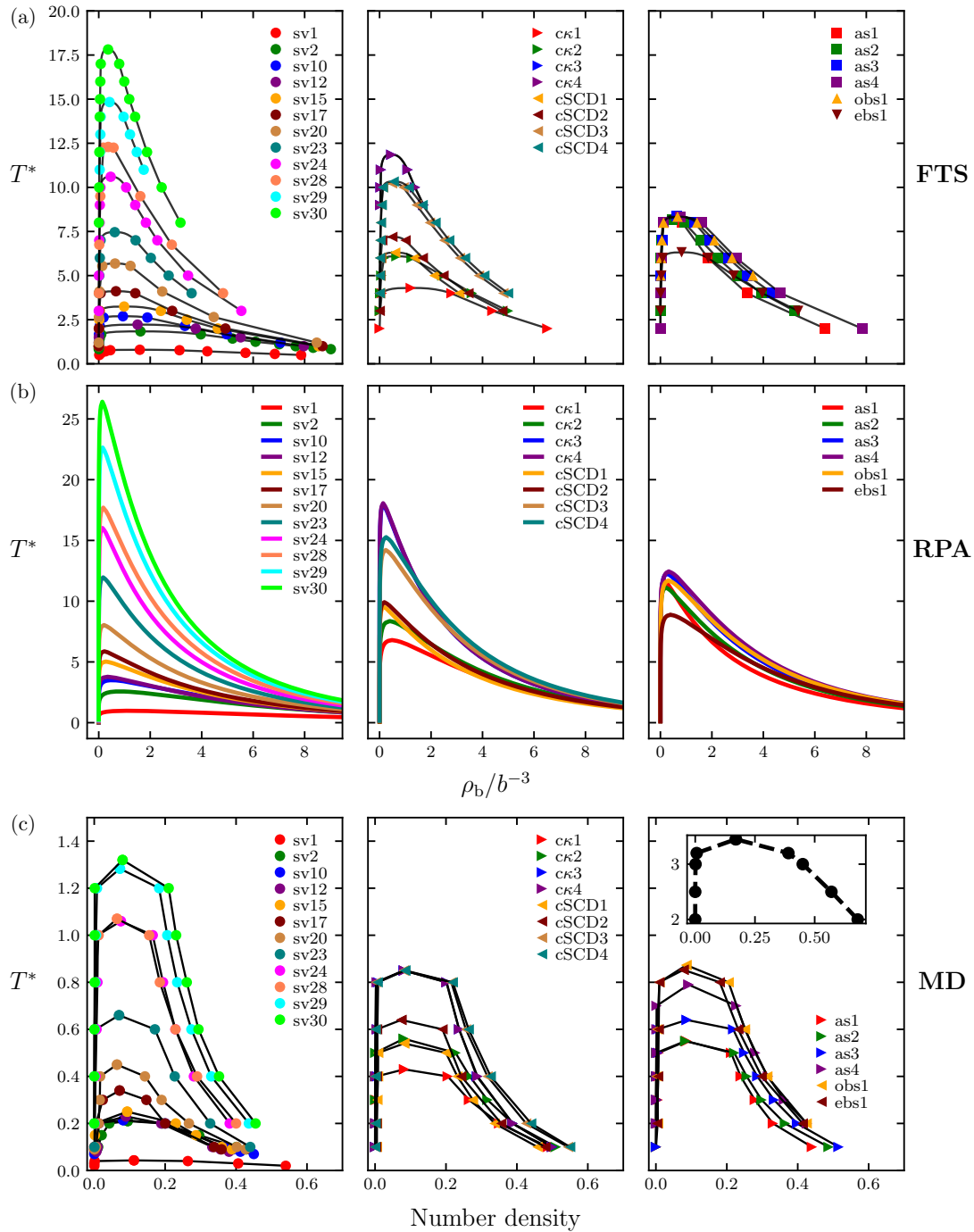


Fig. S2: Phase diagrams of all 26 polyampholytes we consider in the FTS, RPA, and MD models. The phase diagram for the baseline homopolymer model in MD is shown as an inset in the bottom-right panel. Results in maintext Fig. 1d,e are included here as well for completeness and to facilitate comparison.

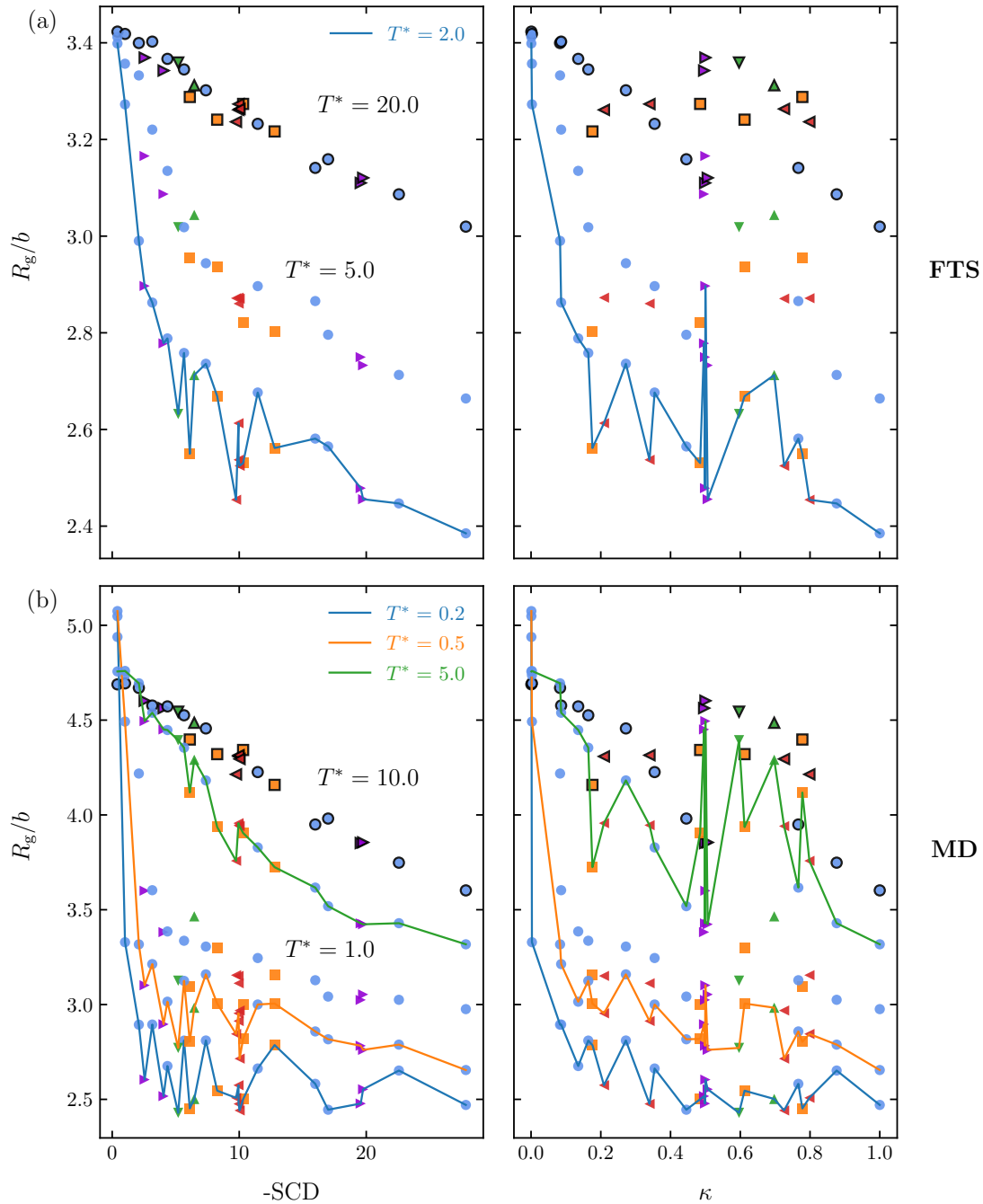


Fig. S3: Variation of polyampholyte root-mean-square radius of gyration in the FTS (top) and MD (bottom) models with SCD (left), κ (right), and temperature (as indicated). Unless specified otherwise, root-mean-square radius of gyration, $\sqrt{R_g^2}$, is denoted simply as R_g for notational simplicity in the present study. Results in maintext Fig. 2a,b,e,f are included here as well to facilitate comparison.

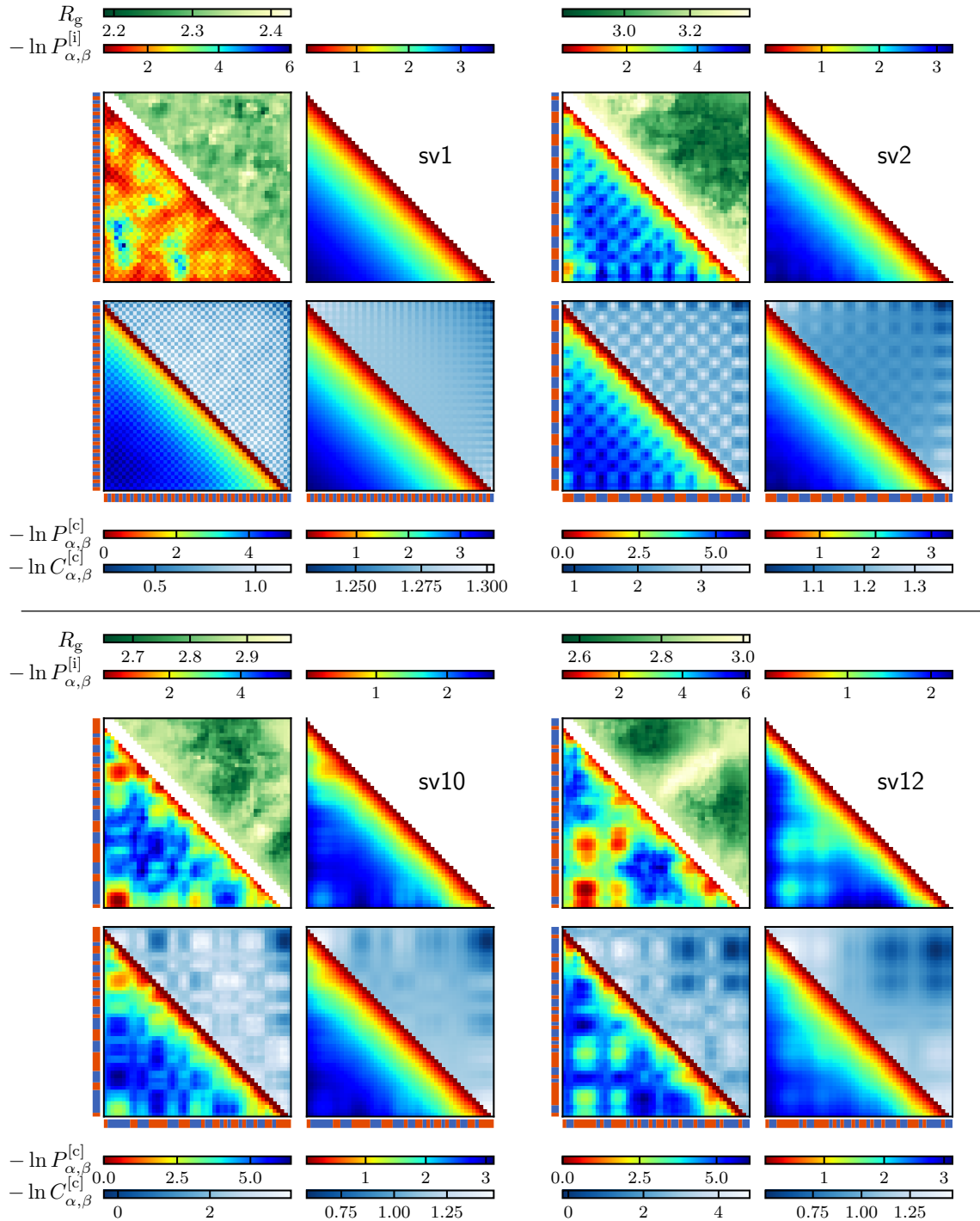


Fig. S4: Contact patterns of polyampholytes as an isolated chain versus in the multiple-chain condensed phase. Results are presented in the same style as that in maintext Fig. 3b,c for the sequence obs1. The corresponding results for all the other 25 polyampholyte sequences are provided here. To facilitate comparison, the obs1 contact patterns in maintext Fig. 3b,c are shown here again as the last item in this supporting figure (1st page, *to be cont'd*).

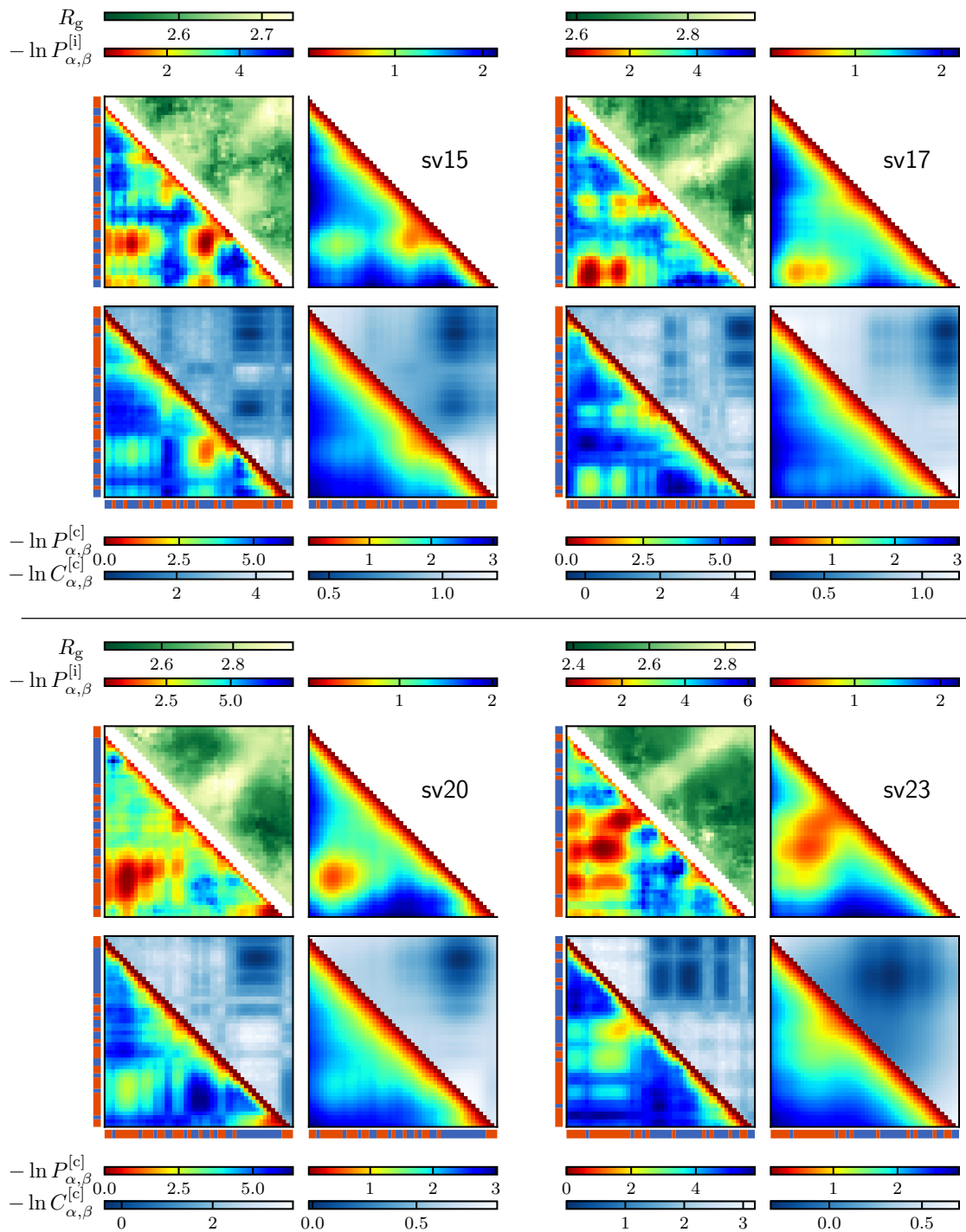


Fig. S4: (2nd page, *cont'd*).

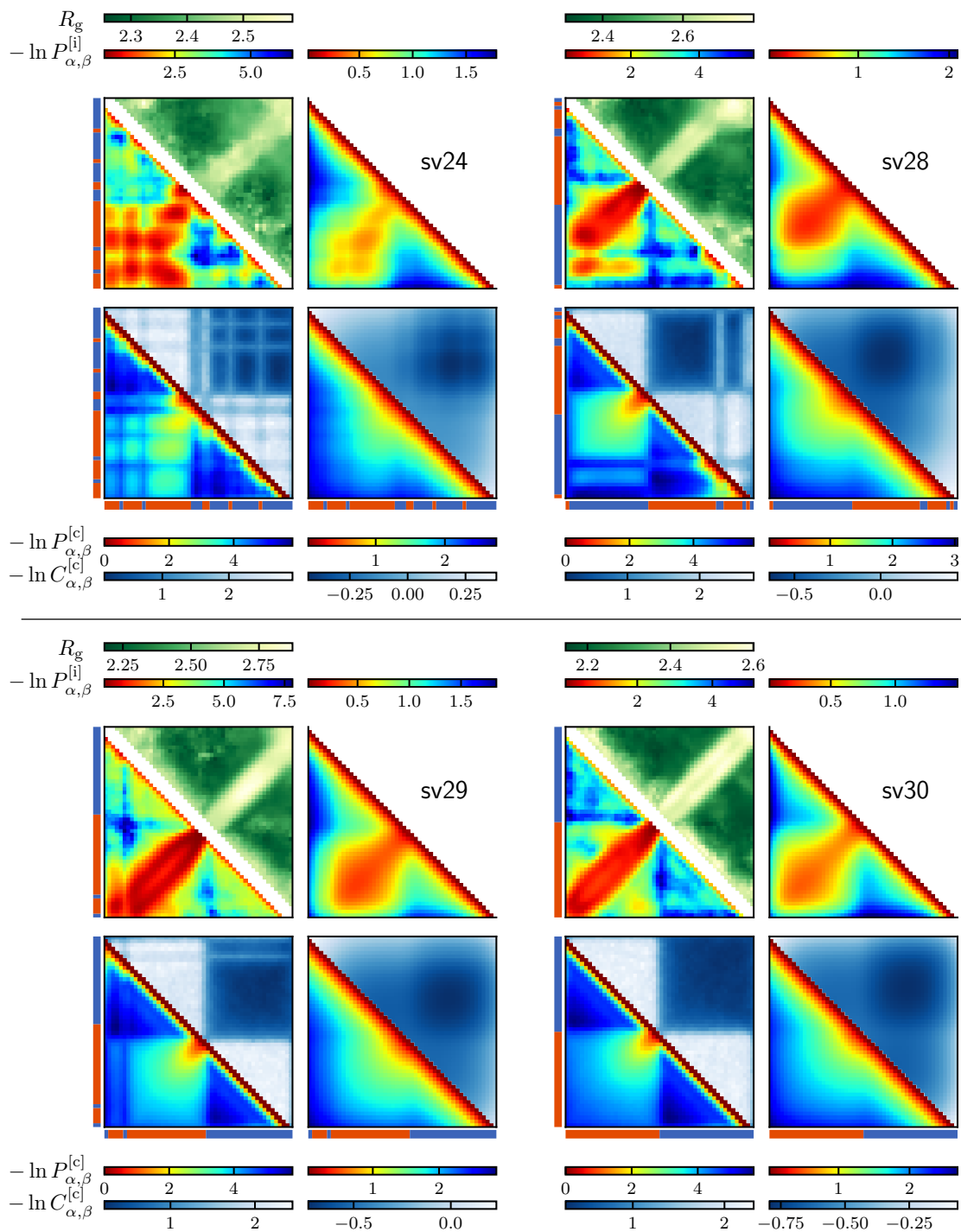


Fig. S4: (3rd page, *cont'd*).

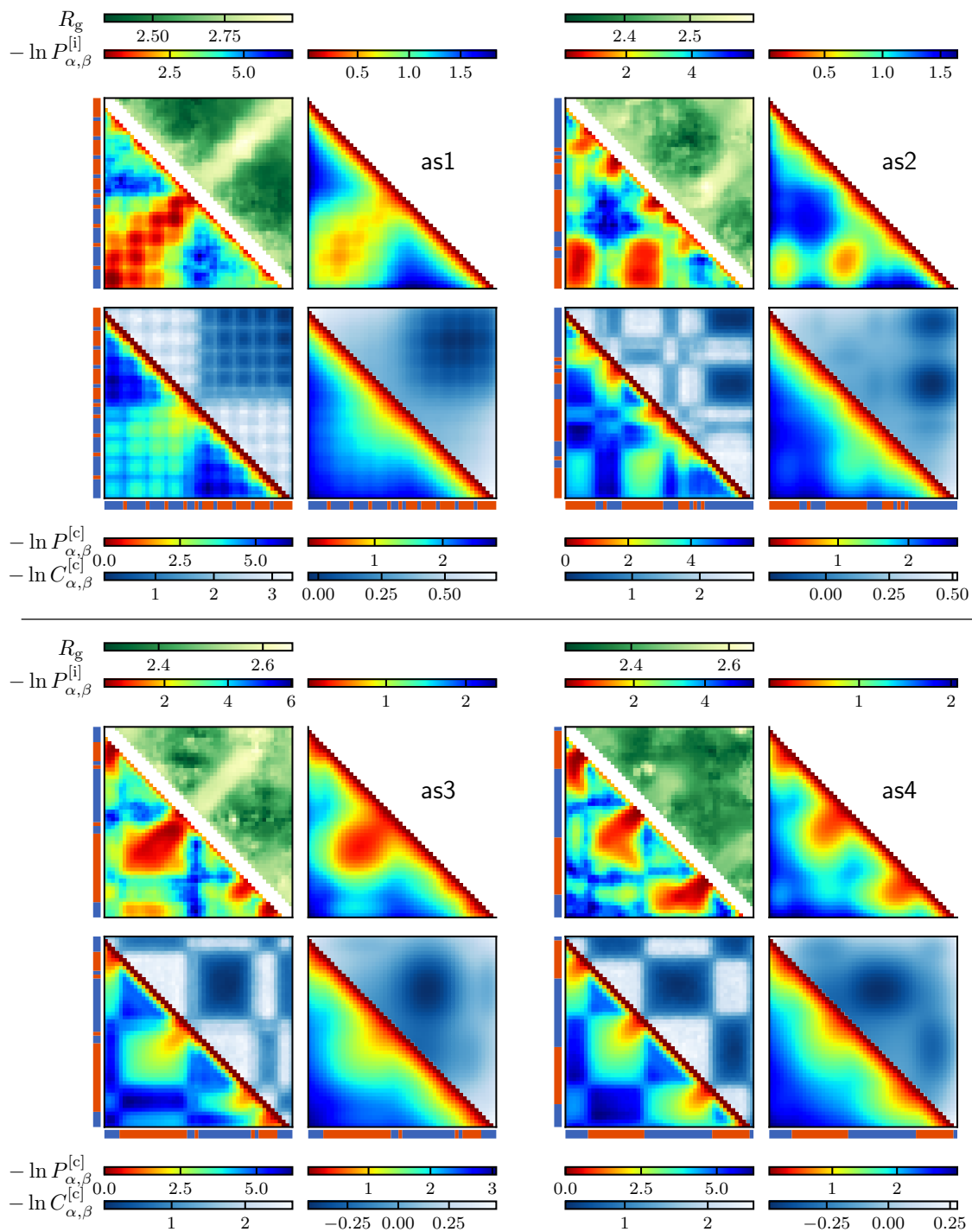


Fig. S4: (4th page, *cont'd*).

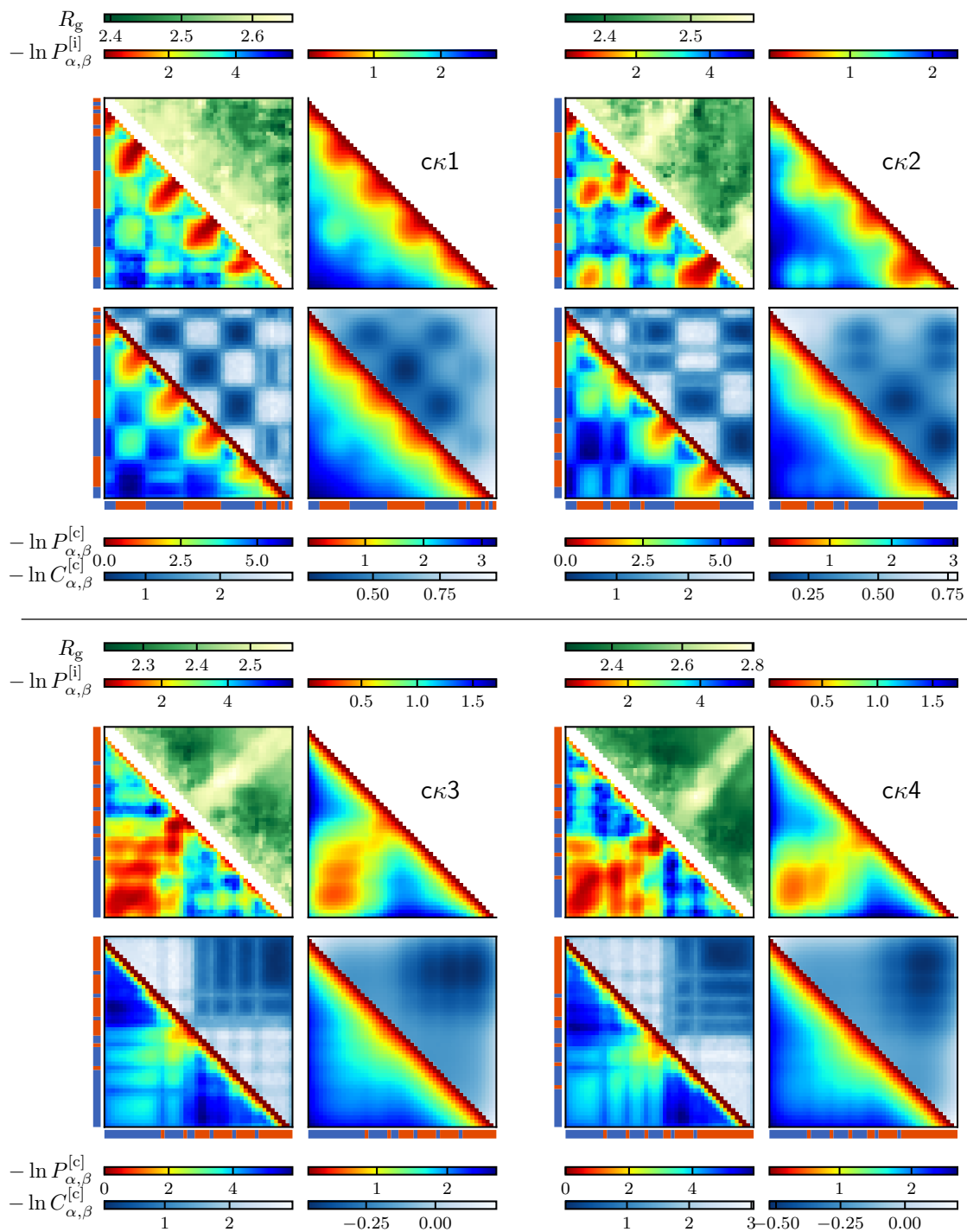


Fig. S4: (5th page, *cont'd*).

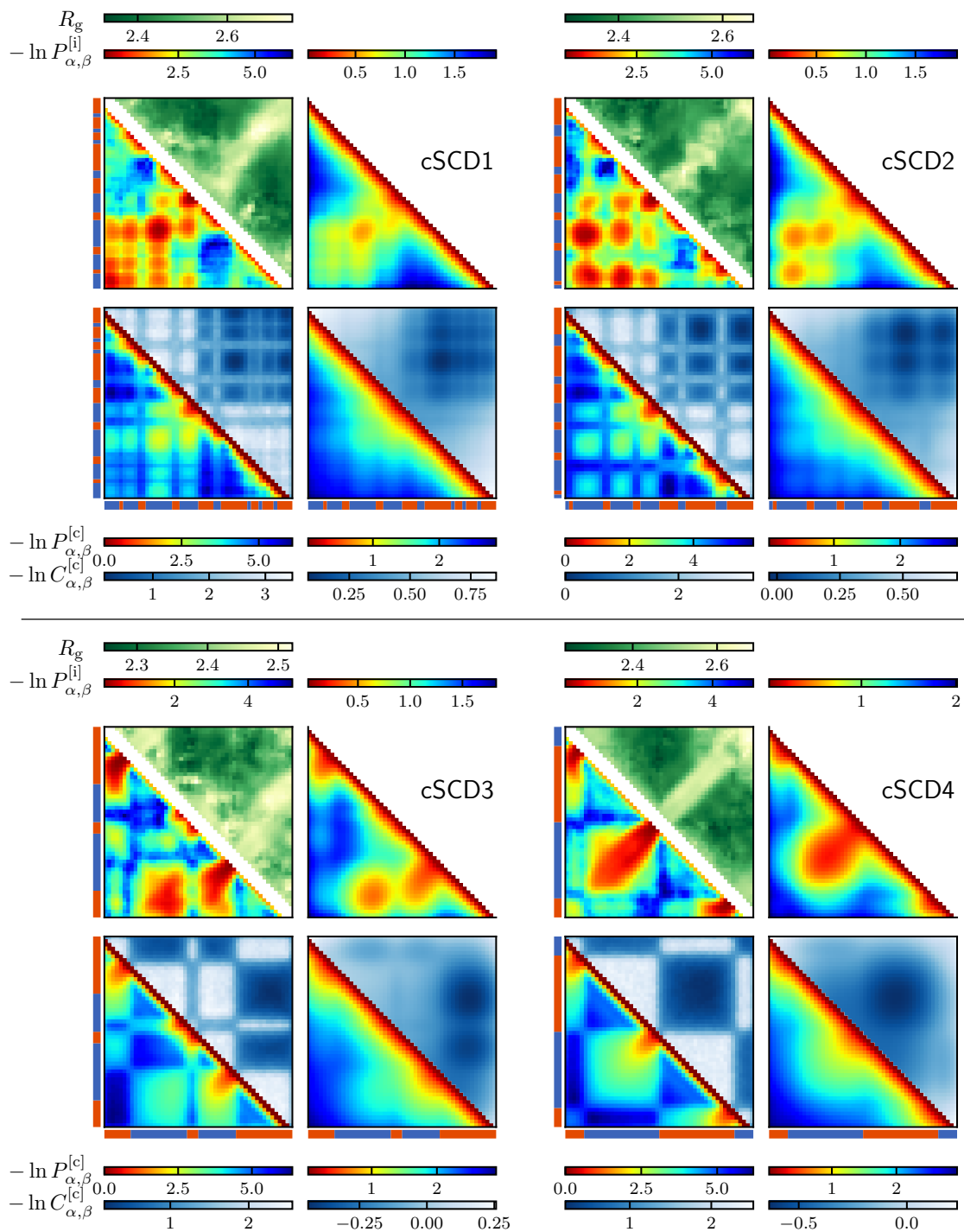


Fig. S4: (6th page, *cont'd*).

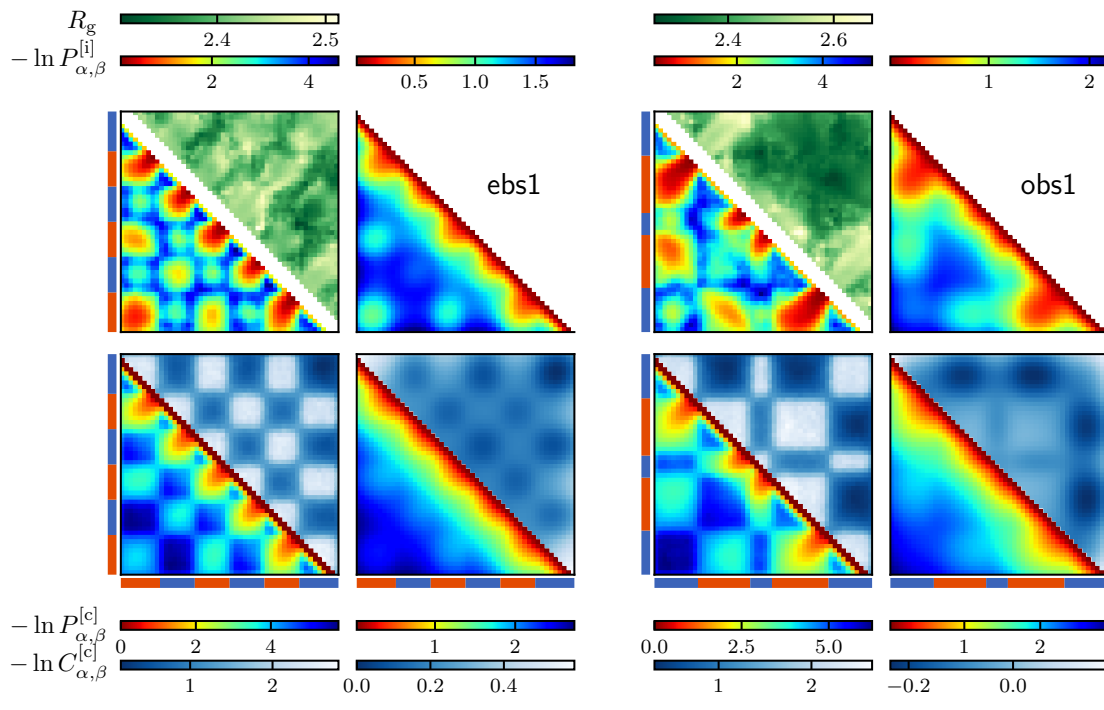


Fig. S4: (7th page, *cont'd*). This is the last page of this supporting figure.

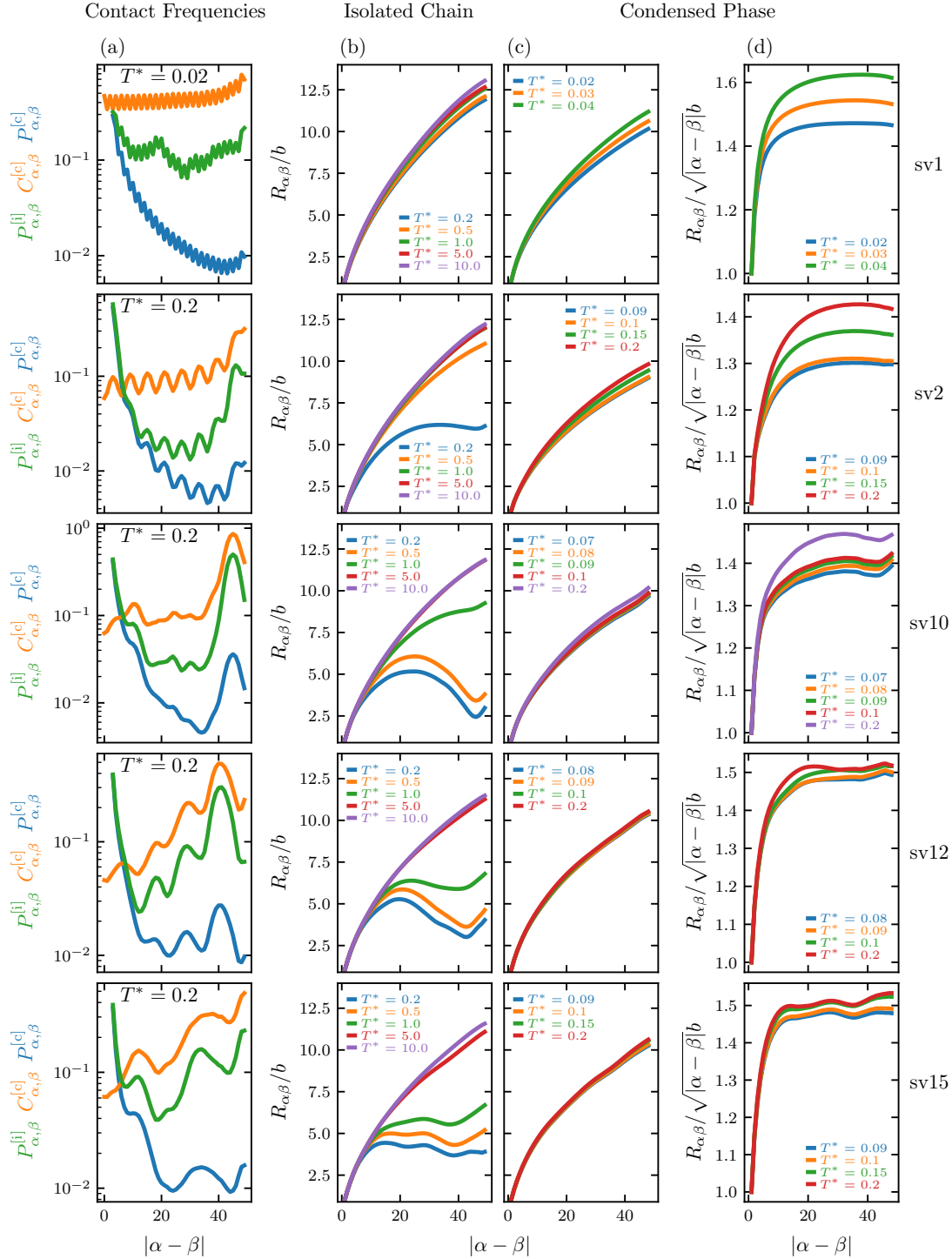


Fig. S5: Intrachain and interchain contact frequencies and intrachain root-mean-square distance $R_{\alpha\beta}$ of polyampholytes, in essentially the same style as that in maintext Fig. 3e–g for the sequence obs1. The corresponding results for all the other 25 polyampholyte sequences are provided here. The data here in columns (a) and (b) for other sequences correspond, respectively, to the contact frequency data in maintext Fig. 3e and 3f. Similarly, the data here in columns (c) and (d) correspond, respectively, to the $R_{\alpha\beta}$ and $R_{\alpha\beta}/\sqrt{|\alpha - \beta|}$ data in maintext Fig. 3g, with the dashed curves in Fig. 3g now replaced by solid curves in column (d). In (d), positive slopes at large $|\alpha - \beta|$ observed for some sequences such as sv28, sv29, sv30, as1, $c\kappa$ 4, and cSCD1 indicate that their condensed-phase conformations are more expanded than Gaussian chains (1st page, *to be cont'd*).

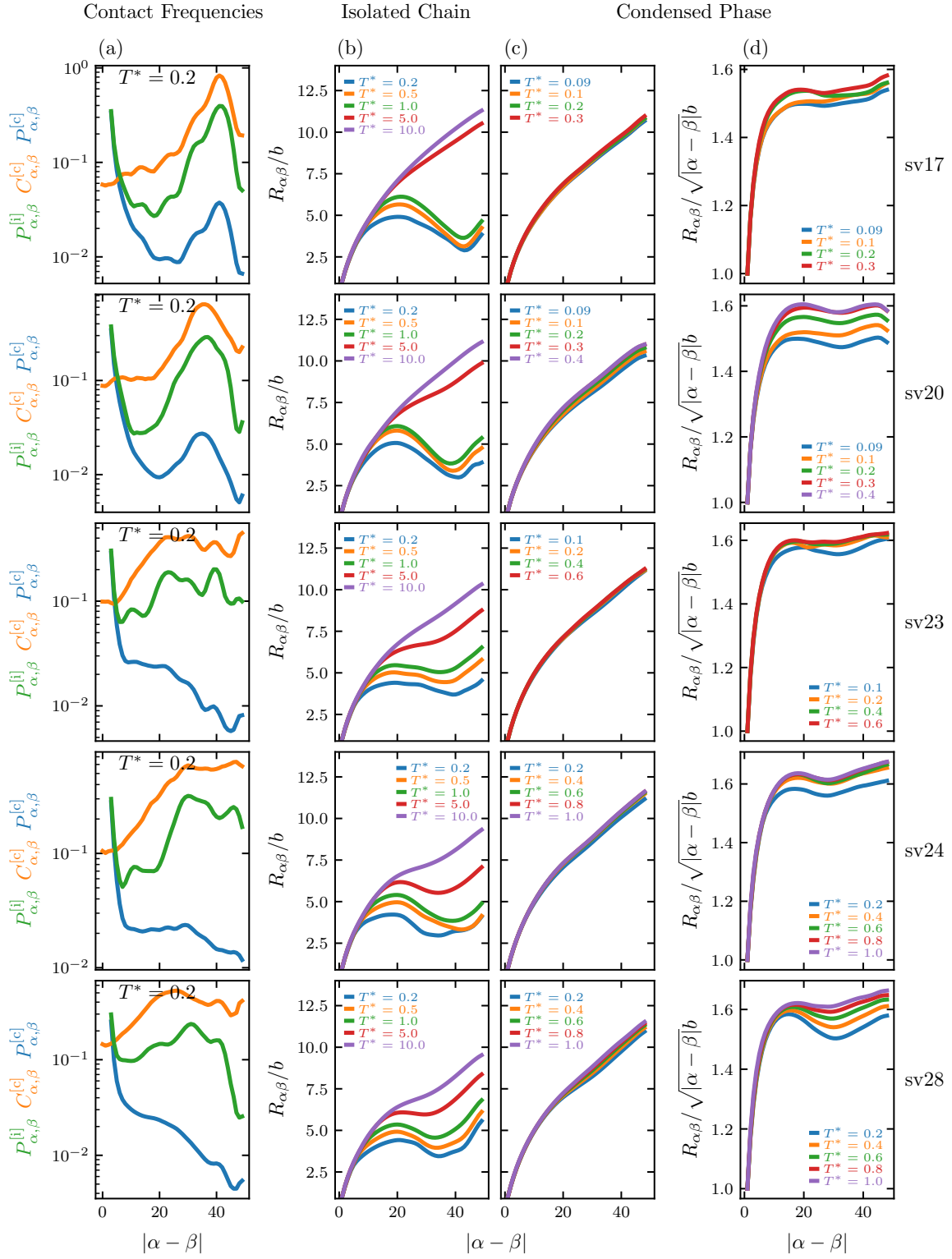


Fig. S5: (2nd page, *cont'd*).

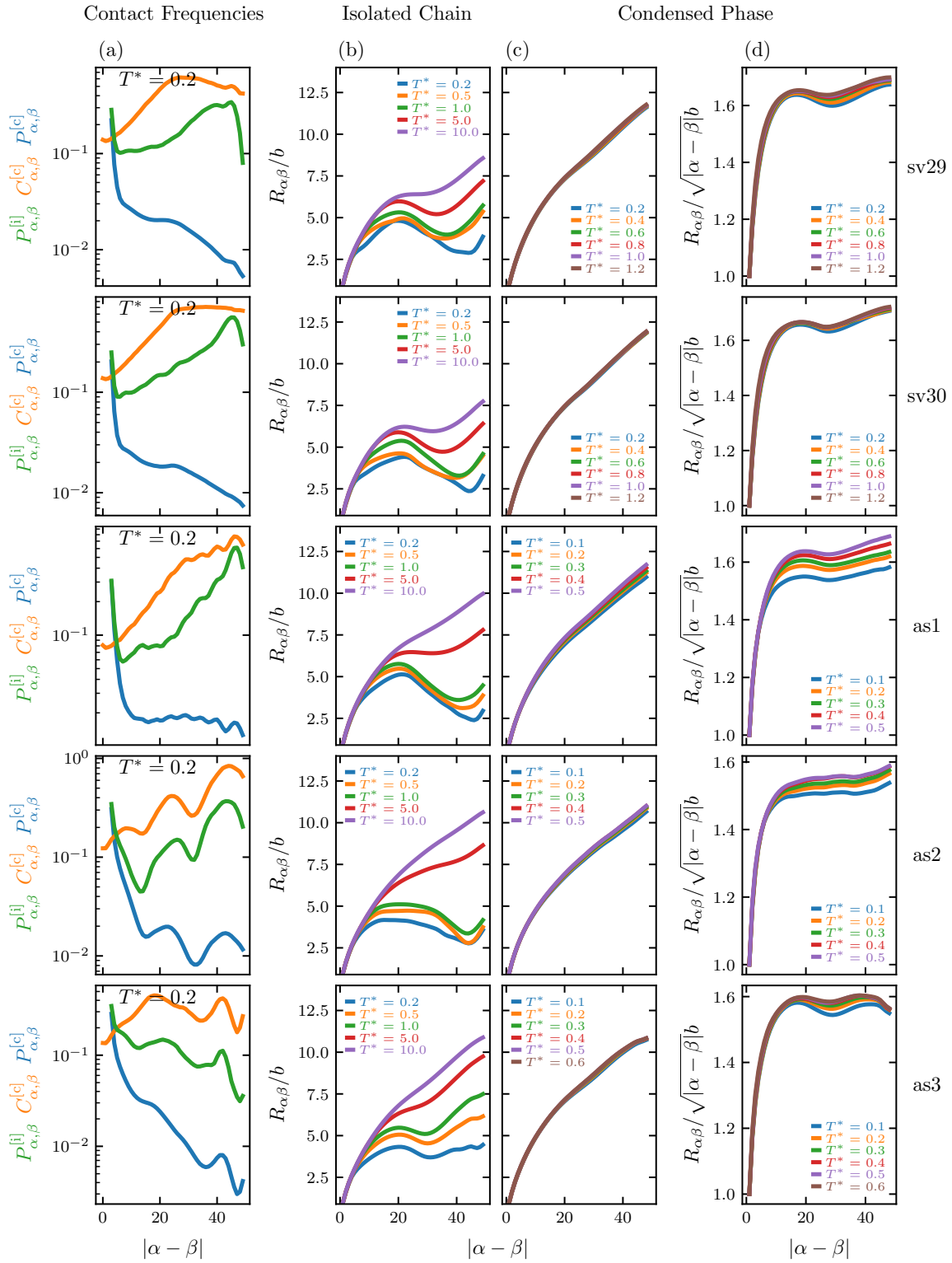


Fig. S5: (3rd page, *cont'd*).

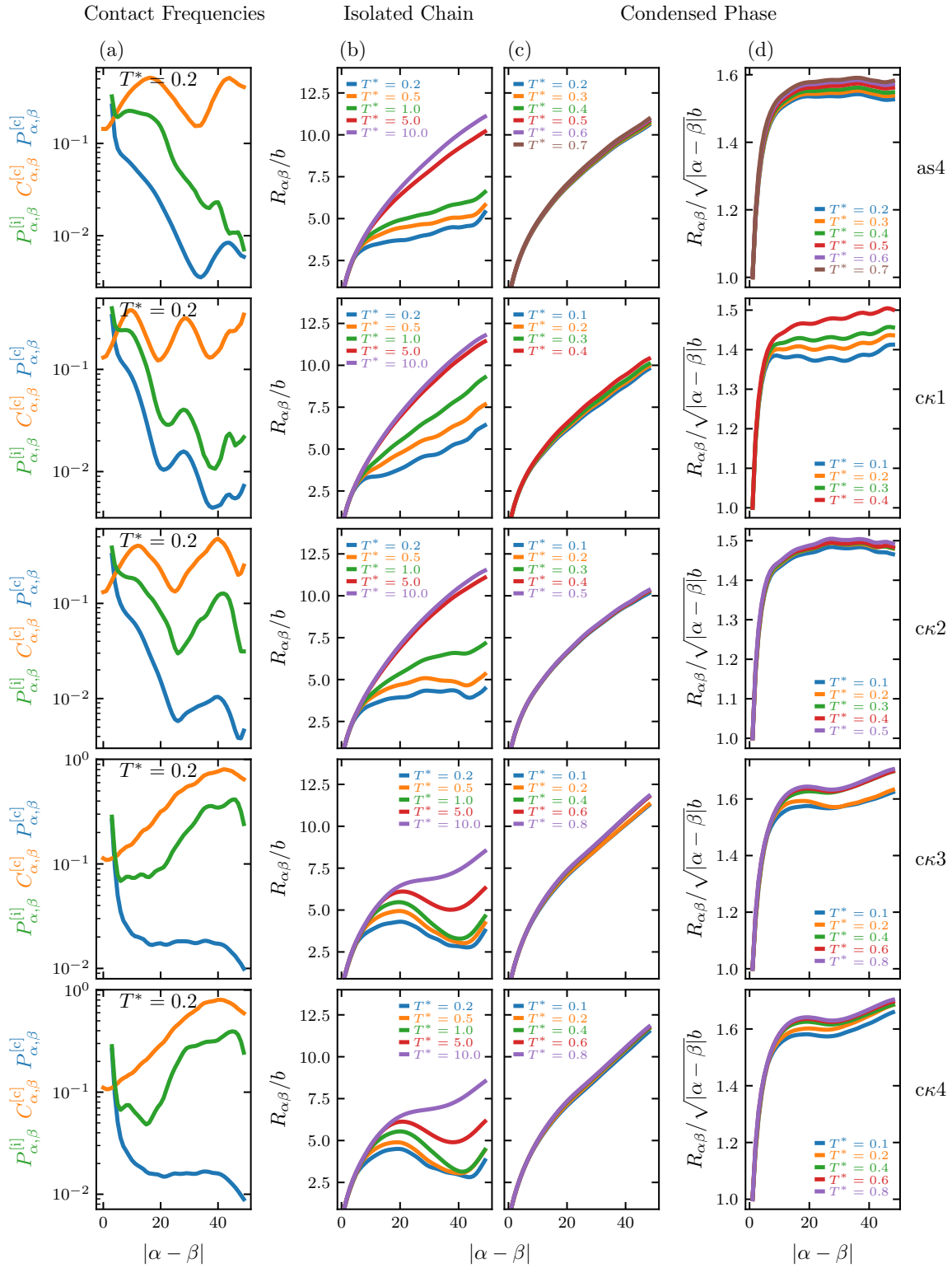


Fig. S5: (4th page, *cont'd*).

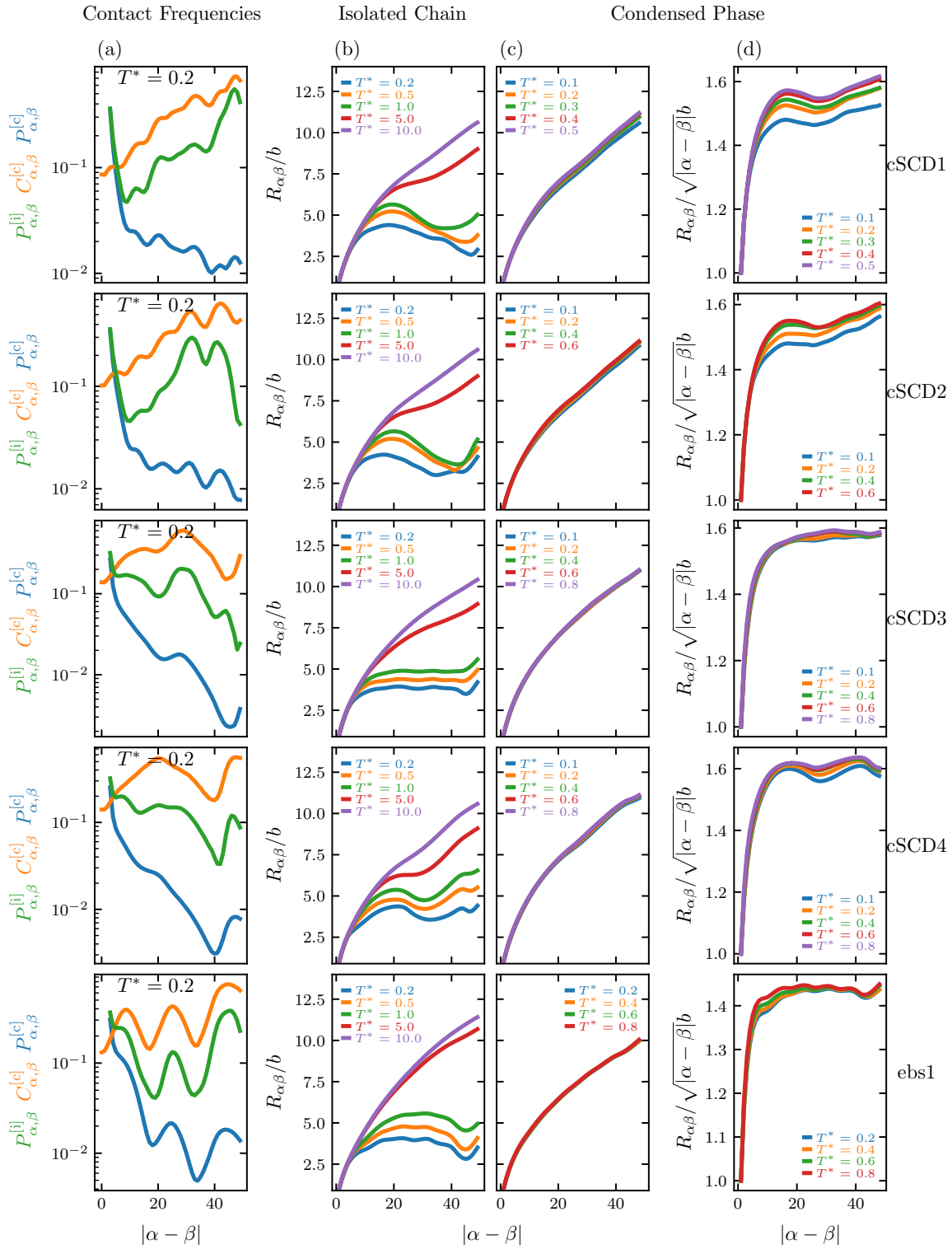


Fig. S5: (5th page, *cont'd*). This is the last page of this supporting figure.

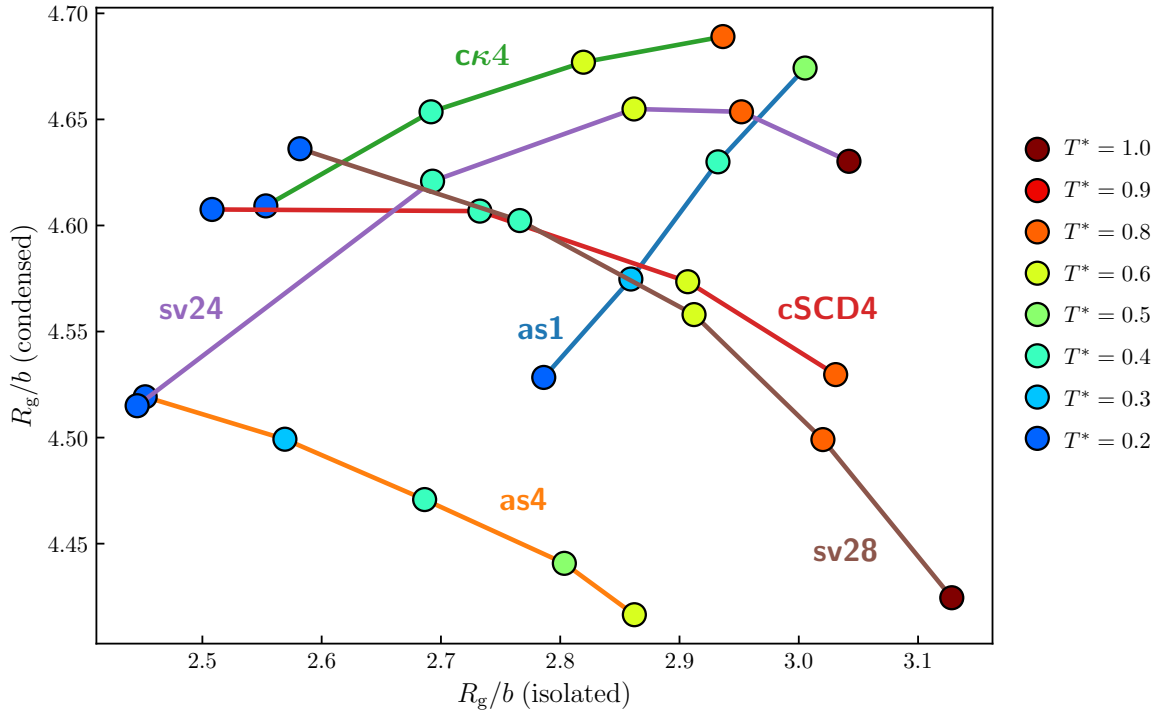


Fig. S6: Temperature- and sequence-pattern-dependent relationship between root-mean-square radii of gyration of isolated versus condensed-phase polyampholyte chains in the MD model. Temperatures for root-mean-square R_g values are color-coded as indicated on the right. Datapoints for the same polyampholyte sequence (as labeled in different colors) are connected by lines with matching color. Lines are otherwise merely guides for the eye. Note that the range of R_g variation in the condensed phase ($\sim 0.3b$, vertical axis) is small compared to the corresponding variation for isolated chains ($\sim 0.7b$, horizontal axis). Whereas isolated-chain R_g s uniformly increase with increasing T^* , condensed-phase R_g s for different sequences can increase or decrease (albeit only slightly) with increasing T^* . The physical origin of this sequence-specific feature and its possible biophysical ramifications should be further investigated in future studies.

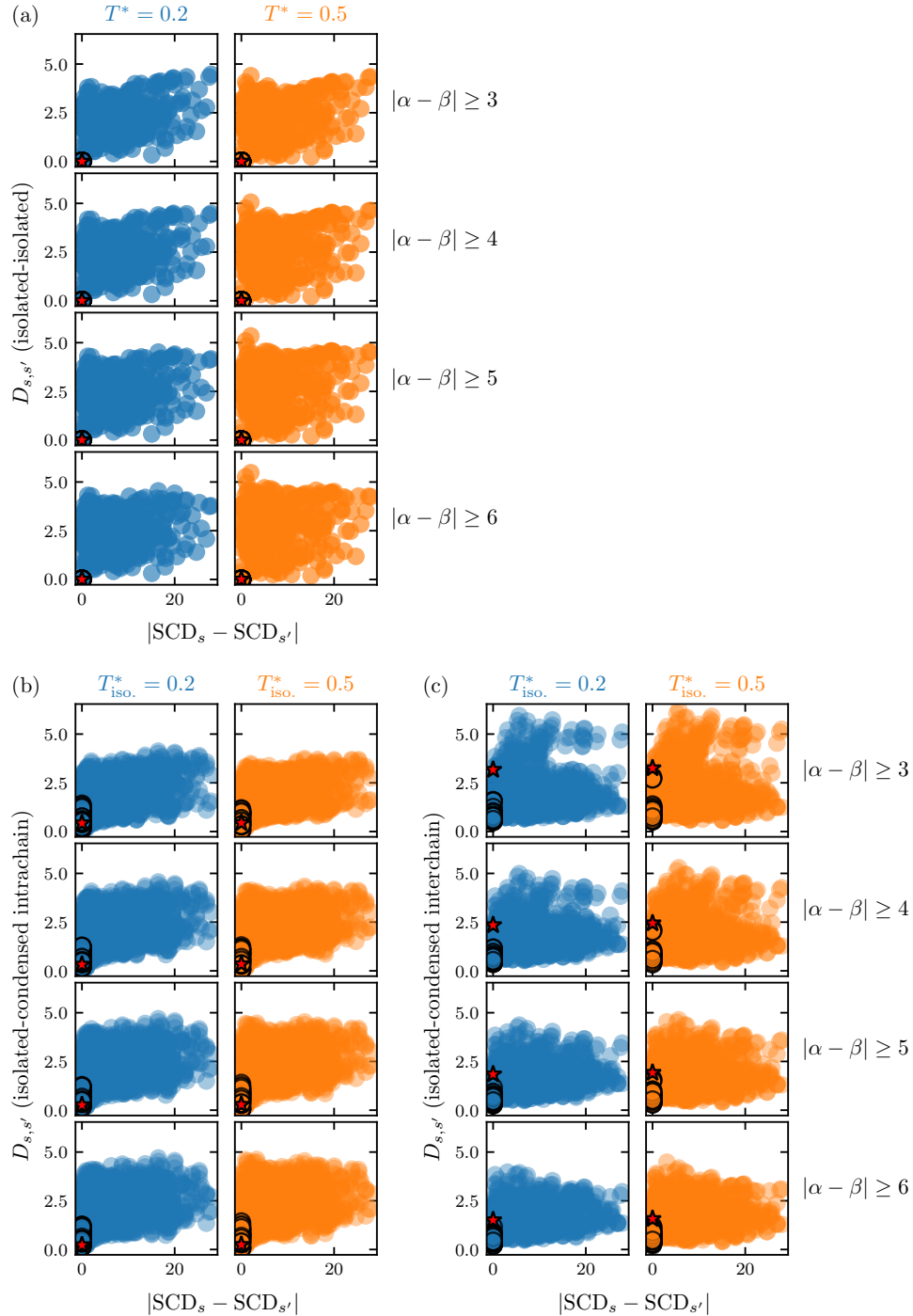


Fig. S7: Comparing contact patterns in the MD model using symmetrized Kullback-Leibler divergences. (a) $D_{s,s'}$ between the $|\alpha - \beta| \geq d_m$ intrachain contacts of two separately isolated polyampholyte sequences s and s' versus $s-s'$ SCD difference ($s, s' =$ all 26 sequences in Fig. S1). Results are shown for two temperatures $T^* = 0.2$ and 0.5 and different cutoffs $d_m = 3-6$ for local contacts, with $s = s'$ datapoints identified by black circles and the value for baseline homopolymer at $T^* = 2.0$ shown as a red star. (b,c) Same as maintext Fig. 4a and Fig. 4b (which are for $T_{\text{iso.}}^* = 0.2$ and $d_m = 4$), respectively, now including data also for $T_{\text{iso.}}^* = 0.5$ and $d_m = 3, 5$, and 6 .

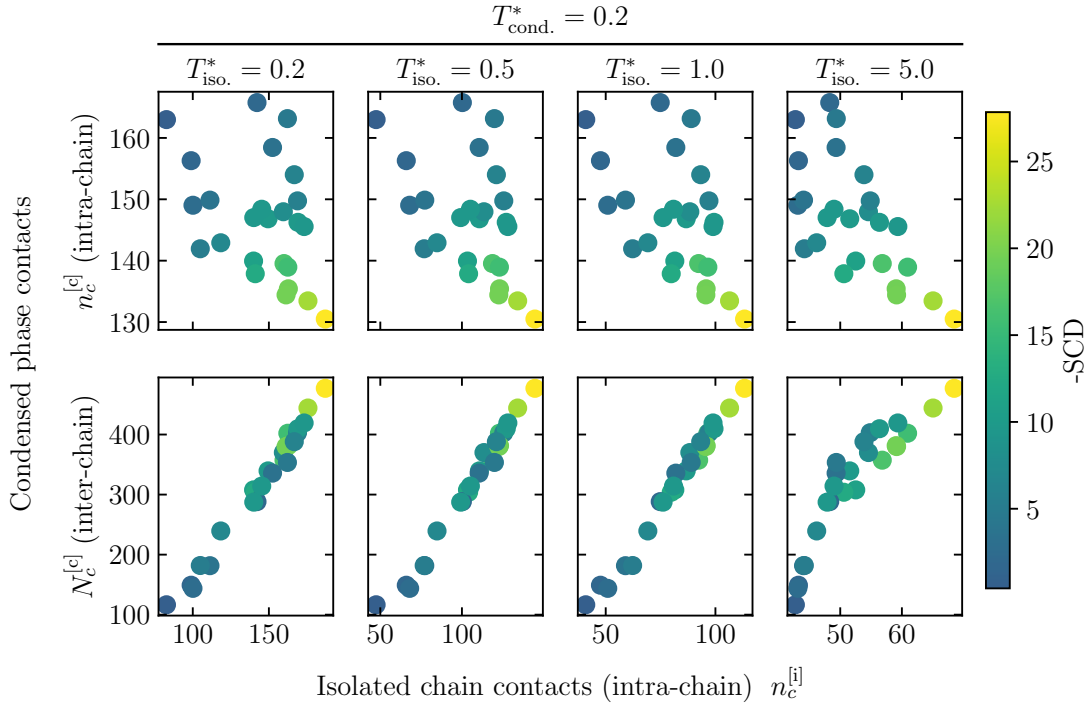


Fig. S8: Variation in the number of isolated-chain intrachain contacts $n_c^{[i]}$ (horizontal axes) with the number of condensed-phase intrachain contacts $n_c^{[c]}$ (vertical axis, top panels) and the number of condensed-phase interchain contacts $N_c^{[c]}$ (vertical axis, bottom panels) in the MD model. Results are present in the same style as that for maintext Fig. 4c,d. In addition to the $T_{\text{iso.}}^* = 0.2$ data in maintext Fig. 4c,d, corresponding data for $T_{\text{iso.}}^* = 0.5, 1.0, \text{ and } 5.0$ are also provided here.

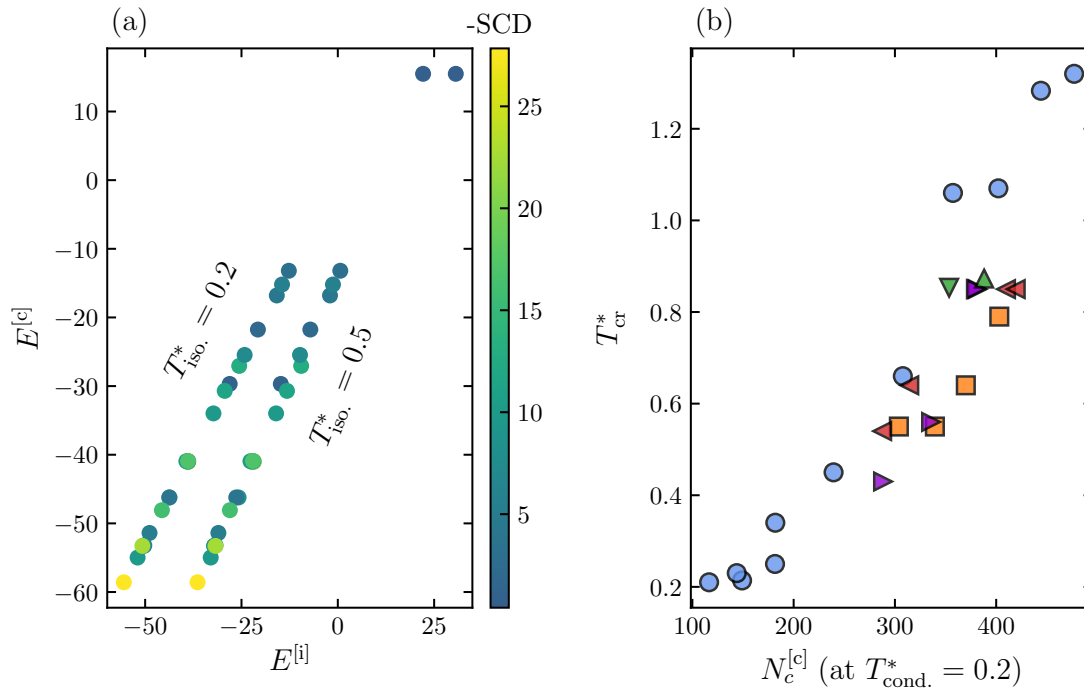


Fig. S9: Relationship between condensed-phase contact frequencies and interaction energies with phase-separation propensity in the MD model. (a) Scatter plots of isolated-chain and condensed-phase potential energies $E^{[i]}$ and energies $E^{[c]}$ (both in units of ϵ) at two simulation temperatures as indicated. The $T_{iso.}^* = 0.2$ datapoints are identical to those provided in maintext Fig. 4e, and are included here to facilitate comparison with the $T_{iso.}^* = 0.5$ datapoints. (b) Critical temperature T_{cr}^* for all sequences except sv1 in maintext Fig. 1b and Fig. S1. Symbols for sequences are the same as those in maintext Fig. 1a.

References

- ¹ Shin, Y.; Brangwynne, C. P. Liquid phase condensation in cell physiology and disease. *Science* **2017**, *357*, eaaf4382.
- ² Lyon, A. S.; Peebles, W. B.; Rosen, M. K. A framework for understanding the functions of biomolecular condensates across scales. *Nat. Rev. Mol. Cell Biol.* **2021**, *22*, 215–235.
- ³ Pappu, R. V.; Cohen, S. R.; Dar, F.; Farag, M.; Kar, M. Phase transitions of associative biomacromolecules. *Chem. Rev.* **2023**, *123*, 8945–8987.
- ⁴ Shen, Z.; Jia, B.; Xu, Y.; Wessén, J.; Pal, T.; Chan, H. S.; Du, S.; Zhang, M. Biological condensates form percolated networks with molecular motion properties distinctly different from dilute solutions. *eLife* **2023** *12*, 81907.
- ⁵ Zhou, H.-X.; Kota, D.; Qin, S.; Prasad, R. Fundamental aspects of phase-separated biomolecular condensates. *Chem. Rev.* **2024**, *124*, 8550–8595.
- ⁶ Nott, T. J.; Petsalaki, E.; Farber, P.; Jervis, D.; Fussner, E.; Plochowietz, A.; Craggs, T. D.; Bazett-Jones, D. P.; Pawson, T.; Forman-Kay, J. D., et al. Phase transition of a disordered nuage protein generates environmentally responsive membraneless organelles. *Mol. Cell* **2015**, *57*, 936–947.
- ⁷ Lin, Y.-H.; Forman-Kay, J. D.; Chan, H. S. Sequence-specific polyampholyte phase separation in membraneless organelles. *Phys. Rev. Lett.* **2016**, *117*, 178101.
- ⁸ Bremer, A.; Farag, M.; Borchers, W. M.; Peran, I.; Martin, E. W.; Pappu, R. V.; Mittag, T. Deciphering how naturally occurring sequence features impact the phase behaviours of disordered prion-like domains. *Nat. Chem.* **2022**, *14*, 196–207.
- ⁹ Vernon, R. M.; Chong, P. A.; Tsang, B.; Kim, T. H.; Bah, A.; Farber, P.; Lin, H.; Forman-Kay, J. D. Pi-Pi contacts are an overlooked protein feature relevant to phase separation. **2018**, *eLife* *7*, e31486.
- ¹⁰ Chen, T.; Song, J.; Chan, H. S. Theoretical perspectives on nonnative interactions and intrinsic disorder in protein folding and binding. *Curr. Opin. Struct. Biol.* **2015**, *30*, 32–42.
- ¹¹ Bauer, D. J.; Stelzl, L. S.; Nikoubashman, A. Single-chain and condensed-state behavior of hnRNPA1 from molecular simulations. *J. Chem. Phys.* **2022** *157*, 154903.
- ¹² Hazra, M. K.; Levy, Y. Cross-talk of cation- π interactions with electrostatic and aromatic interactions: A salt-dependent trade-off in biomolecular condensates. *J. Phys. Chem. Lett.* **2023**, *14*, 8460–8469.
- ¹³ Das, R. K.; Pappu, R. V. Conformations of intrinsically disordered proteins are influenced by linear sequence distributions of oppositely charged residues. *Proc. Natl. Acad. Sci. U.S.A.* **2013**, *110*, 13392–13397.
- ¹⁴ Sawle, L.; Ghosh, K. A theoretical method to compute sequence dependent configurational properties in charged polymers and proteins. *J. Chem. Phys.* **2015**, *143*, 085101.
- ¹⁵ Welsh, T. J.; Krainer, G.; Espinosa, J. R.; Joseph, J. A.; Sridhar, A.; Jahnel, M.; Arter, W.

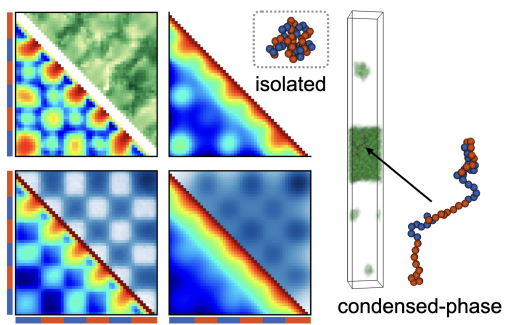
- E.; Saar, K. L.; Alberti, S.; Collepardo-Guevara, R.; Knowles, T. P. J. Surface electrostatics govern the emulsion stability of biomolecular condensates. *Nano Lett.* **2022**, *22*, 612–621.
- ¹⁶ Lyons, H.; Veettil, R. T.; Pradhan, P.; Fomero, C.; De La Cruz, N.; Ito, K.; Eppert, M.; Roeder, R. G.; Sabari, B. R. Functional partitioning of transcriptional regulators by patterned charge blocks. *Cell* **2023**, *186*, 327–345.
- ¹⁷ Flory, P. J.; Fox, T. G., Jr. Treatment of intrinsic viscosities. *J. Am. Chem. Soc.* **1951**, *73*, 1904–1908.
- ¹⁸ Shultz, A. R.; Flory, P. J. Phase equilibria in polymer-solvent systems. *J. Am. Chem. Soc.* **1952**, *74*, 4760–4767.
- ¹⁹ Qian, D.; Michaels, T. C. T.; Knowles, T. P. J. Analytical solution to the Flory-Huggins model. *J. Phys. Chem. Lett.* **2022**, *13*, 7853–7860.
- ²⁰ Panagiotopoulos, A. Z.; Wong, V.; Floriano, M. A. Phase equilibria of lattice polymers from histogram reweighting Monte Carlo simulations. *Macromolecules* **1998**, *31*, 912–918.
- ²¹ Wang, R.; Wang, Z.-G. Theory of polymer chains in poor solvent: Single-chain structure, solution thermodynamics, and Θ point. *Macromolecules* **2014**, *47*, 4094–4102.
- ²² Lin, Y.-H.; Chan, H. S. Phase separation and single-chain compactness of charged disordered proteins are strongly correlated. *Biophys. J.* **2017**, *112*, 2043–2046.
- ²³ Dignon, G. L.; Zheng, W.; Best, R. B.; Mittal, J. Relation between single-molecule properties and phase behavior of intrinsically disordered proteins. *Proc. Natl. Acad. Sci. U.S.A.* **2018**, *115*, 9929–9934.
- ²⁴ Amin, A. N.; Lin, Y.-H.; Das, S.; Chan, H. S. Analytical theory for sequence-specific binary fuzzy complexes of charged intrinsically disordered proteins. *J. Phys. Chem. B* **2020**, *124*, 6709–6720.
- ²⁵ Riback, J. A.; Katanski, C. D.; Kear-Scott, J. L.; Pilipenko, E. V.; Rojek, A. E.; Sosnick, T. R.; Drummond, D. A. Stress-triggered phase separation is an adaptive, evolutionarily tuned response. *Cell* **2017**, *168*, 1028–1040.
- ²⁶ von Bülow, S.; Tesei, G.; Lindorff-Larsen, K. Prediction of phase separation propensities of disordered proteins from sequence. bioRxiv – The Preprint Server for Biology, Cold Spring Harbor Laboratory, <https://doi.org/10.1101/2024.06.03.597109> (accessed 2024-07-24).
- ²⁷ McCarty, J.; Delaney, K. T.; Danielsen, S. P. O.; Fredrickson, G. H.; Shea, J.-E. Complete phase diagram for liquid-liquid phase separation of intrinsically disordered proteins. *J. Phys. Chem. Lett.* **2019**, *10*, 1644–1652.
- ²⁸ Danielsen, S. P. O.; McCarty, J.; Shea, J.-E.; Delaney, K. T.; Fredrickson, G. H. Molecular design of self-coacervation phenomena in block polyampholytes. *Proc. Natl. Acad. Sci. U.S.A.* **2019**, *116*, 8224–8232.
- ²⁹ Wessén, J., Pal, T., Das, S., Lin, Y.-H. & Chan, H. S. A simple explicit-solvent model of polyampholyte phase behaviors and its ramifications for dielectric effects in biomolecular condensates. *J. Phys. Chem. B* **2021** *125*, 4337–4358.
- ³⁰ Pal, T.; Wessén, J.; Das, S.; Chan, H. S. Subcompartmentalization of polyampholyte species in organelle-like condensates is promoted by charge-pattern mismatch and strong excluded-volume

- interaction. *Phys. Rev. E* **2021**, **103**, 042406.
- ³¹ Dill, K. A. Dominant forces in protein folding. *Biochemistry* **1990**, *29*, 7133-7155.
- ³² Chan, H. S.; Dill, K. A. The effects of internal constraints on the configurations of chain molecules. *J. Chem. Phys.* **1990**, *92*, 3118–3135. Erratum: *J. Chem. Phys.* **1997**, *107*, 10353.
- ³³ Dill, K. A.; Fiebig, K. M.; Chan, H. S. Cooperativity in protein folding kinetics. *Proc. Natl. Acad. Sci. U.S.A.* **1993**, *90*, 1942–1946.
- ³⁴ Plaxco, K. W.; Simons, K. T.; Baker, D. Contact order, transition state placement and the refolding rates of single domain proteins. *J. Mol. Biol.* **1998**, *277*, 985–994.
- ³⁵ Chan, H. S. Protein folding: Matching speed and locality. *Nature* **1998**, *392*, 761–763.
- ³⁶ Chan, H. S.; Zhang, Z.; Wallin, S.; Liu, Z. Cooperativity, local-nonlocal coupling, and nonnative interactions: Principles of protein folding from coarse-grained models. *Annu. Rev. Phys. Chem.* **2011**, *62*, 301–326.
- ³⁷ Das, S.; Amin, A. N.; Lin, Y.-H.; Chan, H. S. Coarse-grained residue-based models of disordered protein condensates: Utility and limitations of simple charge pattern parameters. *Phys. Chem. Chem. Phys.* **2018**, *20*, 28558–28574.
- ³⁸ Camargo-Molina, J. E., Mandal, T., Pasechnik, R. & Wessén, J. Heavy charged scalars from $c\bar{s}$ fusion: a generic search strategy applied to a 3HDM with $U(1) \times U(1)$ family symmetry. *Journal of High Energy Physics (JHEP)* **2018**, *2018*, 24.
- ³⁹ Wang, F. & Landau, D. P. Efficient, multiple-range random walk algorithm to calculate the density of states. *Phys. Rev. Lett.* **2001**, *86*, 2050–2053.
- ⁴⁰ Hazra, M. K.; Levy, Y. Charge pattern affects the structure and dynamics of polyampholyte condensates. *Phys. Chem. Chem. Phys.* **2020**, *22*, 19368–19375.
- ⁴¹ Devarajan, D. S.; Wang, J.; Szała-Mendyk, B.; Rekhi, S.; Nikoubashman, A.; Kim, Y. C.; Mittal, J. Sequence-dependent material properties of biomolecular condensates and their relation to dilute phase conformations. *Nat. Comm.* **2024**, *15*, 1912.
- ⁴² Rana, U.; Wingreen, N. S.; Brangwynne, C. P.; Panagiotopoulos, A. Z. Interfacial exchange dynamics of biomolecular condensates are highly sensitive to client interactions. *J. Chem. Phys.* **2024**, *160*, 145102.
- ⁴³ Ruff, K. M. Predicting conformational properties of intrinsically disordered proteins from sequence. *Methods Mol. Biol.* **2021**, *2141*, 347–389.
- ⁴⁴ Cohan, M. C.; Shinn, M. K.; Lalmansingh, J. M.; Pappu, R. V. Uncovering non-random binary patterns within sequences of intrinsically disordered proteins. *J. Mol. Biol.* **2022**, *434*, 167373.
- ⁴⁵ Huihui, J.; Firman, T.; Ghosh, K. Modulating charge patterning and ionic strength as a strategy to induce conformational changes in intrinsically disordered proteins. *J. Chem. Phys.* **2018**, *149*, 085101.
- ⁴⁶ Wang, J.; Choi, J. M.; Holehouse, A. S.; Lee, H. O.; Zhang, X.; Jahnelt, M.; Maharana, S.; Lemaitre, R.; Pozniakovskiy, A.; Drechsel, D., et al. A molecular grammar governing the driving forces for phase separation of prion-like RNA binding proteins. *Cell* **2018**, *174*, 688–699.
- ⁴⁷ Zheng, W.; Dignon, G.; Brown, M.; Kim, Y. C.; Mittal, J. Hydrophathy patterning complements charge patterning to describe conformational preferences of disordered proteins. *J. Phys. Chem.*

- Lett.* **2020**, *11*, 3408–3415.
- ⁴⁸ Wessén, J.; Das, S.; Pal, T.; Chan, H. S. Analytical formulation and field-theoretic simulation of sequence-specific phase separation of protein-like heteropolymers with short- and long-spatial-range interactions. *J. Phys. Chem. B* **2022**, *126*, 9222–9245. Correction: *J. Phys. Chem. B* **2023**, *127*, 11100.
- ⁴⁹ Rekhi, S.; Devarajan, D. S.; Howard, M. P.; Kim, Y. C.; Nikoubashman, A.; Mittal, J. Role of strong localized vs. weak distributed interactions in disordered protein phase separation. *J. Phys. Chem. B* **2023**, *127*, 3829–3838.
- ⁵⁰ Rekhi, S.; Garcia, C. C.; Barai, M.; Rizuan, A.; Schuster, B. S.; Kiick, K.; Mittal, J. Expanding the molecular language of protein liquid-liquid phase separation. *Nat. Chem.* **2024**, *16*, 1113–1124.
- ⁵¹ Lin, Y.-H.; Brady, J. P.; Chan, H. S.; Ghosh, K. A unified analytical theory of heteropolymers for sequence-specific phase behaviors of polyelectrolytes and polyampholytes. *J. Chem. Phys.* **2020**, *152*, 045102.
- ⁵² Lin, Y.-H.; Kim, T. H.; Das, S.; Pal, T.; Wessén, J.; Rangadurai, A. K.; Kay, L. E.; Forman-Kay, J. D.; Chan, H. S. Electrostatics of salt-dependent reentrant phase behaviors highlights diverse roles of ATP in biomolecular condensates. arXiv – Quantitative Biology (q-bio), Biomolecules (Cornell University) <https://arxiv.org/abs/2401.04873> (accessed 2024-07-24).
- ⁵³ Mahdi, K. A.; Olvera de la Cruz, M. Phase diagrams of salt-free polyelectrolyte semidilute solutions. *Macromolecules* **2000**, *33*, 7649–7654.
- ⁵⁴ Ermoshkin, A. V.; Olvera de la Cruz, M. A modified random phase approximation of polyelectrolyte solutions. *Macromolecules* **2003**, *36*, 7824–7832.
- ⁵⁵ Cheong, D. W.; Panagiotopoulos, A. Z. Phase behaviour of polyampholyte chains from grand canonical Monte Carlo simulations. *Mol. Phys.* **2005**, *103*, 3031–3044.
- ⁵⁶ Fredrickson, G. H. *The Equilibrium Theory of Inhomogeneous Polymers*. Oxford University Press, Oxford, U.K. (2006).
- ⁵⁷ Sing, C. E.; Perry, S. L. Recent progress in the science of complex coacervation. *Soft Matter* **2020**, *16*, 2885–2914.
- ⁵⁸ Jacobs, W. M. Theory and simulation of multiphase coexistence in biomolecular mixtures. *J. Chem. Theory Comput.* **2023**, *19*, 3429–3445.
- ⁵⁹ Parisi, G. On complex probabilities. *Phys. Lett. B* **1983**, *131*, 393–395.
- ⁶⁰ Klauder, J. R. A Langevin approach to fermion and quantum spin correlation functions. *J. Phys. A: Math. Gen.* **1983**, *16*, L317–L319.
- ⁶¹ Sillmore, K. S.; Howard, M. P.; Panagiotopoulos, A. Z. Vapour–liquid phase equilibrium and surface tension of fully flexible lennard–jones chains. *Mol. Phys.* **2017**, *115*, 320–327.
- ⁶² Dignon, G. L.; Zheng, W.; Kim, Y. C.; Best, R. B.; Mittal, J. Sequence determinants of protein phase behavior from a coarse-grained model. *PLoS Comput. Biol.* **2018**, *14*, e1005941.
- ⁶³ Das, S.; Lin, Y.-H.; Vernon, R. M.; Forman-Kay, J. D.; Chan, H. S. Comparative roles of charge, π , and hydrophobic interactions in sequence-dependent phase separation of intrinsically

- disordered proteins. *Proc. Natl. Acad. Sci. U.S.A.* **2020**, *117*, 28795–28805.
- ⁶⁴ Joseph, J. A.; Reinhardt, A.; Aguirre, A.; Chew, P. Y.; Russell, K. O.; Espinosa, J. R.; Garaizar, A.; Collepardo-Guevara, R. Physics-driven coarse-grained model for biomolecular phase separation with near-quantitative accuracy. *Nat. Comput. Sci.* **2021**, *1*, 732–743.
- ⁶⁵ Tesei, G.; Schulze, T. K.; Crehuet, R.; Lindorff-Larsen, K. Accurate model of liquid-liquid phase behavior of intrinsically disordered proteins from optimization of single-chain properties. *Proc. Natl. Acad. Sci. U.S.A.* **2021**, *118*, e2111696118.
- ⁶⁶ Fredrickson, G. H.; Ganesan, V.; Drolet, F. Field-theoretic computer simulation methods for polymers and complex fluids. *Macromolecules* **2022**, *35*, 16–39.
- ⁶⁷ Riggleman, R. A., Kumar, R. & Fredrickson, G. H. Investigation of the interfacial tension of complex coacervates using field-theoretic simulations. *J. Chem. Phys.* **2012**, *136*, 024903.
- ⁶⁸ Lin, Y.-H.; Wessén, J.; Pal, T.; Das, S.; Chan, H.S. Numerical techniques for applications of analytical theories to sequence-dependent phase separations of intrinsically disordered proteins. *Methods Mol. Biol.* **2023**, *2563*, 51–94.
- ⁶⁹ Flory, P. J. The configuration of real polymer chains. *J. Chem. Phys.* **1949**, *17*, 303–310.
- ⁷⁰ Wang, J.; Devarajan, D. S.; Nikoubashman, A.; Mittal, J. Conformational properties of polymers at droplet interfaces as model systems for disordered proteins. *ACS Macro Lett.* **2023**, *12*, 1472–1478.
- ⁷¹ Farag, M.; Borchers, W. M.; Bremer, A.; Mittag, T.; Pappu, R. V. Phase separation of protein mixtures is driven by the interplay of homotypic and heterotypic interactions. *Nat. Comm.* **2023**, *14*, 5527.
- ⁷² Johnson, C. N.; Sojitra, K. A.; Sohn, E. J.; Moreno-Romero, A. K.; Baudin, A.; Xu, X.; Mittal, J.; Libich, D. S. Insights into molecular diversity within the FUS/EWS/TAF15 protein family: Unraveling phase separation of the N-terminal low-complexity domain from RNA-binding protein EWS. *J. Am. Chem. Soc.* **2024**, *146*, 8071–8085.
- ⁷³ Wang, J.; Devarajan, D. S.; Kim, Y. C.; Nikoubashman, A.; Mittal, J. Sequence-dependent conformational transitions of disordered proteins during condensation. bioRxiv – The Preprint Server for Biology, Cold Spring Harbor Laboratory, <https://doi.org/10.1101/2024.01.11.575294> (accessed 2024-07-24).
- ⁷⁴ Kullback, S.; Leibler, R. A. On information and sufficiency. *Ann. Math. Statist.* **1951**, *22*, 79–86.
- ⁷⁵ Song, J.; Li, J.; Chan, H. S. Small-angle X-ray scattering signatures of conformational heterogeneity and homogeneity of disordered protein ensembles. *J. Phys. Chem. B* **2021**, *125*, 6451–6478.
- ⁷⁶ Tesei, G.; Trolle, A. I.; Jonsson, N.; Betz, J.; Knudsen, F. E.; Pesce, F.; Johansson, K. E.; Lindorff-Larsen, K. Conformational ensembles of the human intrinsically disordered proteome. *Nature* **2024**, *626*, 897–904.
- ⁷⁷ Lotthammer, J. M.; Ginell, G. M.; Griffith, D.; Emenecker, R. J.; Holehouse, A. S. Direct prediction of intrinsically disordered protein conformational properties from sequence. *Nat. Methods* **2024**, *21*, 465–476.

- ⁷⁸ Wohl, S.; Zheng, W. Interpreting transient interactions of intrinsically disordered proteins. *J. Phys. Chem. B* **2023**, *127*, 2395–2406.
- ⁷⁹ Huihui, J.; Ghosh, K. Intrachain interaction topology can identify functionally similar intrinsically disordered proteins. *Biophys. J.* **2020**, *120*, 1860–1868.
- ⁸⁰ Devarajan, D. S.; Rekhi, S.; Nikoubashman, A.; Kim, Y. C.; Howard, M. P.; Mittal, J. Effect of charge distribution on the dynamics of polyampholytic disordered proteins. *Macromolecules* **2022**, *55*, 8987–8997.
- ⁸¹ Phan, T. M.; Kim, Y. C.; Debelouchina, G. Y.; Mittal, J. Interplay between charge distribution and DNA in shaping HP1 paralog phase separation and localization. *eLife* **2023**, *12*, RP90820.
- ⁸² Mohanty, P.; Shenoy, J.; Rizuan, A.; Mercado-Ortiz, J. F.; Fawzi, N. L.; Mittal, J. A synergy between site-specific and transient interactions drives the phase separation of a disordered, low-complexity domain. *Proc. Natl. Acad. Sci. U.S.A.* **2023**, *120*, e2305625120.
- ⁸³ Zarin, T.; Strome, B.; Peng, G.; Pritišanac, I.; Forman-Kay, J. D.; Moses, A. M. Identifying molecular features that are associated with biological function of intrinsically disordered protein regions. *eLife* **2021**, *10*, e60220.
- ⁸⁴ Irbäck, A.; Jónsson, S. Æ.; Linnemann, N.; Linse, B.; Wallin, S. Aggregate geometry in amyloid fibril nucleation. *Phys. Rev. Lett.* **2013**, *110*, 058101.
- ⁸⁵ Irbäck, A.; Wessén, J. Thermodynamics of amyloid formation and the role of intersheet interactions. *J. Chem. Phys.* **2015**, *143*, 105104.
- ⁸⁶ Vogel, T.; Li, Y. W.; Wüst, T.; Landau, D. P. Generic, hierarchical framework for massively parallel Wang-Landau sampling. *Phys. Rev. Lett.* **2013**, *110*, 210603.
- ⁸⁷ Khan, M. O.; Kennedy, G.; Chan, D. Y. C. A scalable parallel Monte Carlo method for free energy simulations of molecular systems. *J. Comput. Chem.* **2005**, *26*, 72–77.
- ⁸⁸ Zhan, L. A parallel implementation of the Wang-Landau algorithm. *Comput. Phys. Comm.* **2008**, *179*, 339–344.
- ⁸⁹ Yin, J.; Landau, D. P. Massively parallel Wang-Landau sampling on multiple GPUs. *Comput. Phys. Comm.* **2012**, *183*, 1568–1573.
- ⁹⁰ Wang, Z.-G. Fluctuation in electrolyte solutions: The self energy. *Phys. Rev. E* **2010**, *81*, 021501.
- ⁹¹ Parisi, G.; Wu, Y.-S. Perturbation theory without gauge fixing. *Sci. Sinica* **1981**, *24*, 483–496.
- ⁹² Chan, H. S.; Halpern, M. B. New ghost-free infrared-soft gauges. *Phys. Rev. D* **1986**, *33*, 540–547.
- ⁹³ Lennon, E. M.; Mohler, G. O.; Ceniceros, H. D.; García-Cervera, C. J.; Fredrickson, G. H. Numerical solutions of the complex Langevin equations in polymer field theory. *Multiscale Model. Simul.* **2008**, *6*, 1347–1370.
- ⁹⁴ Itzykson, C.; Zuber, J.-B. *Quantum Field Theory*. McGraw-Hill Inc., New York, NY (1980).



TOC graphics